Green Chemistry

ROYAL SOCIETY OF CHEMISTRY

CRITICAL REVIEW

View Article Online
View Journal | View Issue

Cite this: *Green Chem.*, 2024, **26**, 7478

Deep eutectic solvents as green solvents for materials preparation

Dongkun Yu,[a] Depeng Jiang,[b] Zhimin Xue *[c] and Tiancheng Mu *[d]

The concept of sustainability has progressively evolved into a consensus for achieving long-term development, and the significance of solvents in regard to green chemistry and sustainable processes cannot be underestimated. Hydrogen-bonding interactions and heterogeneity at the nanoscale determine the outstanding solvating properties of deep eutectic solvents (DESs). A relatively wide electrochemical window is the prerequisite for the preparation of more materials (especially active metals) by electrodeposition in these eutectic systems. The role of DESs in the fabrication process may be chemical or physical, although the line between the two is blurred. At times, DESs function as a reducing agent, while in other cases they solely provide a liquid environment to facilitate the reaction. This review provides a set of methodologies to guide the preparation of materials with specific morphology and functions.

Received 10th January 2024,
Accepted 10th May 2024

DOI: 10.1039/d4gc00136b

rsc.li/greenchem

1. Introduction

As a new class of green solvents, deep eutectic solvents (DESs) have attracted much attention in recent years due to their low toxicity, biodegradability and tunable properties. DESs are usually defined as mixtures composed of two or more solid or liquid components that form eutectics at room temperature and can be used as solvents, as can be known from their names.[1] The formation of DESs is based on the eutectic principle, *i.e.*, forming the eutectic mixture with a lower melting point than each single component, in which hydrogen bonding interactions are attributed as the intrinsic driving force.[2,3] Later on, concepts such as eutectic molecular liquids, type V DESs, halogen bonding DESs, supramolecular DESs, and eutectogels were proposed as well.[4–8]

The most common method for preparing DESs involves mixing hydrogen bond donors (HBDs) and hydrogen bond acceptors (HBAs) in specific ratios.[9] HBDs are usually quatern-

[a]*Department of Applied Physics, KTH Royal Institute of Technology, Hannes Alfvéns väg 12, 114 19 Stockholm, Sweden*
[b]*Shanghai Institute of Space Power-Sources, Shanghai 200245, China*
[c]*College of Materials Science and Technology, Beijing Forestry University, Beijing 100083, P. R. China. E-mail: zmxue@bjfu.edu.cn*
[d]*Department of Chemistry, Renmin University of China, Beijing 100872, P. R. China. E-mail: tcmu@ruc.edu.cn*

Dongkun Yu

Dongkun Yu received his MSc degree from Renmin University of China in 2020 under the supervision of Professor Tiancheng Mu. He is currently a PhD candidate at the KTH Royal Institute of Technology, with support from the China Scholarship Council. His research focuses on novel eutectics and natural biopolymers. He has co-authored over thirty peer-reviewed publications.

Depeng Jiang

Depeng Jiang received his Master's degree in Engineering from the Shanghai Academy of Spaceflight Technology in 2007. From 2021 to 2022, he was a visiting scholar at the KTH Royal Institute of Technology. He is currently a senior Engineer in the State Key Laboratory of Shanghai Institute of Space Power-sources. His research interests cover high-efficiency solar cells, photoelectric materials and devices. So far, he has published over 50 professional papers and 4 co-authored monographs. He has obtained 15 national invention patents.

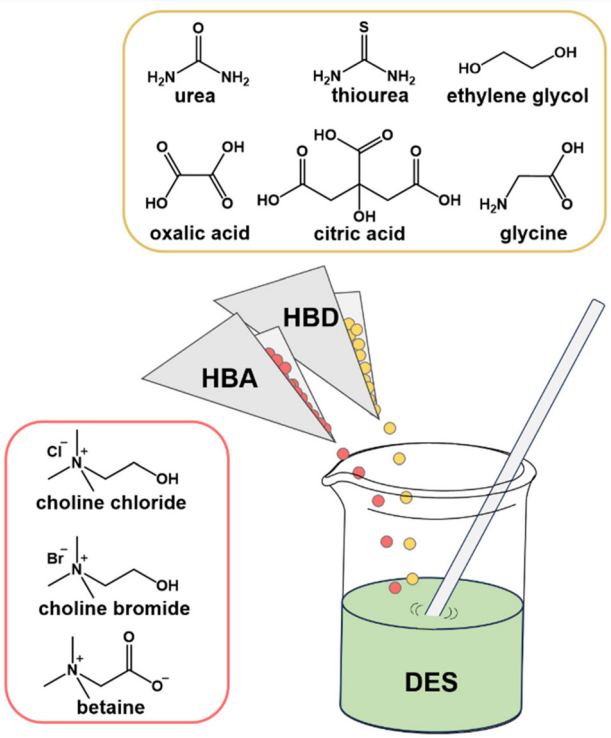

Scheme 1 Examples of typical HBAs and HBDs.

ary ammonium salts or choline derivatives, while HBAs are carboxylic acids, metal salts, or polyols (Scheme 1).[10] When mixed, HBDs and HBAs form hydrogen bonds, resulting in the formation of a eutectic mixture with a lower melting point than either individual component. However, with the deepening of relevant basic research, some other principles have also been discovered, such as the effect of entropy increase.[3,11] The unique properties and potential applications of DESs make them a promising class of green solvents applicable to various fields, including the extraction and separation of biomass, materials preparation, organic chemical synthesis, pharmaceutics, genetic science, *etc*.[12–16]

Currently, DESs occupy a significant position in the synthesis of nanoparticles and nanomaterials. The unique hydrogen-bonding network between components in DESs creates a favorable environment for the nucleation and controlled growth of nanoparticles.[17] This, furthermore, facilitates precise tuning of the size, morphology, and surface properties of nanoparticles, offering great potential for applications in fields such as catalysis and drug delivery, where the properties of nanoparticles play a key role.

Fig. 1 summarizes representative studies of materials prepared using DESs since 2004. Notably, early interest among researchers was directed towards the synthesis of Metal Organic Frameworks (MOFs), which may be related to the hot topics at that time.[18–20] Some endeavours were focused on nanoparticle preparation as well. For instance, Liao *et al.* manipulated the morphology of gold nanoparticles by modulating the water proportion within the DES.[21] It was not until 2017 that research on the mechanism of materials growth began to appear, which may be related to the research progress of neutron scattering technology in DES structure investigation.[22,23] Subsequently, the topic of materials prepared by DES entered a new stage.

Researchers are deeply exploring the possibility of combining DESs with other cutting-edge synthesis techniques such as microwave-assisted synthesis and continuous-flow synthesis.[24,25] This convergence could potentially enable unprecedented efficiencies and scalability in materials production. Furthermore, the application range of DESs has been extended to the synthesis of complex polymers and functional materials, taking full advantage of their intrinsic heterogeneity and macromolecular structures.

Zhimin Xue

Prof. Zhimin Xue received her Ph.D. degree from Renmin University of China in 2014. From 2018 to 2019, she was a visiting associate professor at the University of Tennessee, Knoxville. She is currently a professor at Beijing Forestry University. Her research interests cover the treatment and conversion of biomass, design, and applications of green solvents. Furthermore, she was awarded the Prize of Liangxi Forestry Science and Technology Award and the Science and Technology Award of the China Association for Instrumental Analysis. She was selected for the National High-level Talent Special Support Plan in 2021.

Tiancheng Mu

Prof. Tiancheng Mu received his Ph.D. in physical chemistry from the Institute of Chemistry, the Chinese Academy of Sciences, in 2004. He worked in the Department of Industrial Chemistry, Oldenburg University, as a postdoc from 2005 to 2007. He is currently a full professor in the Department of Chemistry, Renmin University of China. He has authored over 200 peer-reviewed scientific publications and six book chapters. He currently serves as an Associate Editor for RSC Advances, *and as an Advisory Board Member for* CLEAN – Soil, Air, Water. *He is vice-director of the Ionic Liquids Committee of the Chemical Industry and Engineering Society of China.*

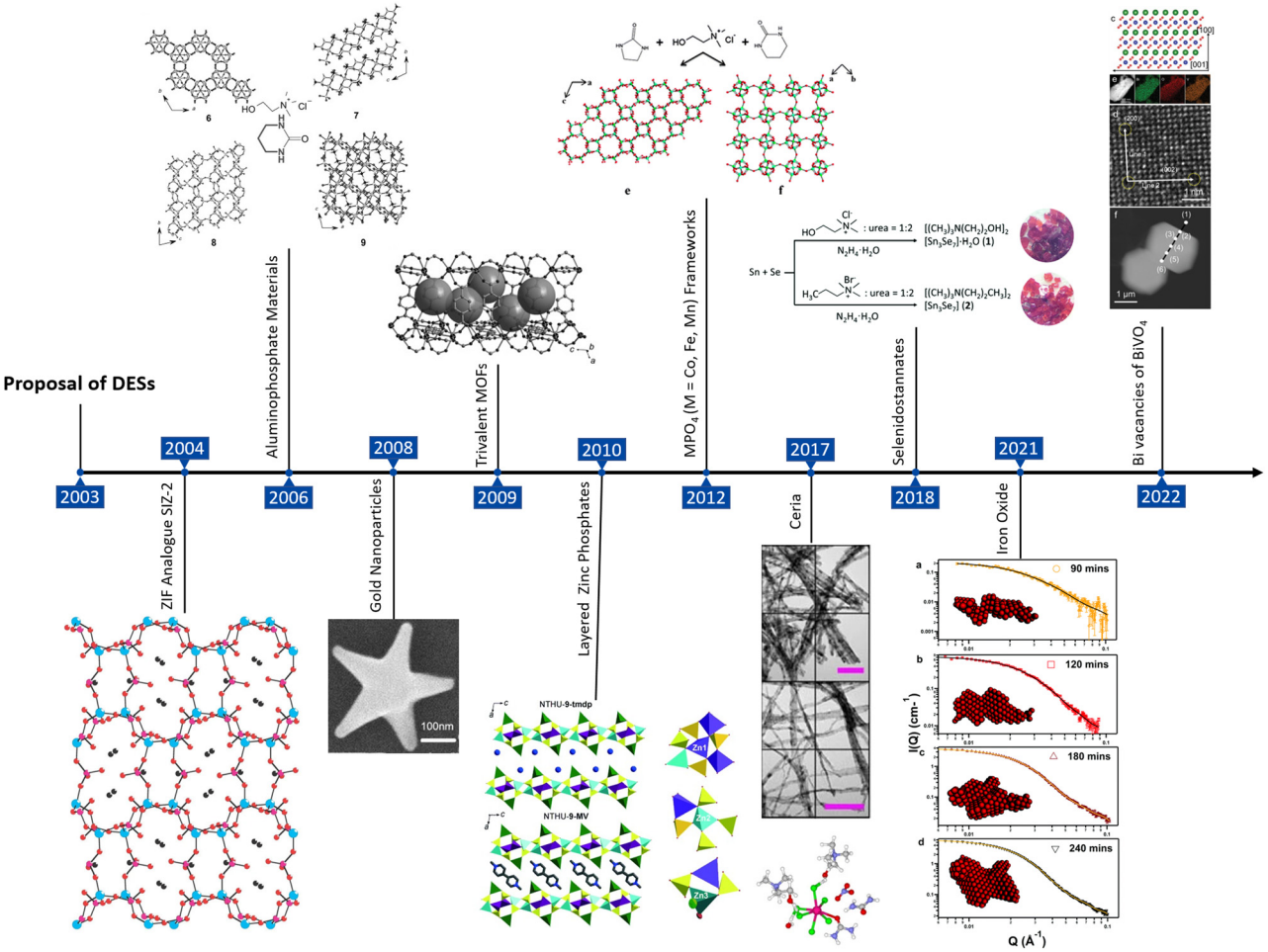

Fig. 1 Schematic graph showing milestone work of materials synthesized using DESs. ZIF analogues SIZ-2,[18] reproduced with permission from ref. 18. Copyright 2004, Nature Publishing Group. Aluminophosphate Materials,[19] reproduced with permission from ref. 19. Copyright 2006, Wiley-VCH. Gold nanoparticles,[21] reproduced with permission from ref. 21. Copyright 2008, Wiley-VCH. Trivalent MOFs,[20] reproduced with permission from ref. 20. Copyright 2009, Wiley-VCH. Layered zinc phosphates,[28] reproduced with permission from ref. 28. Copyright 2010, Wiley-VCH. MPO_4 (M = Co, Fe, Mn) framework,[29] reproduced with permission from ref. 29. Copyright 2012, Royal Society of Chemistry. Ceria,[22] reproduced with permission from ref. 22. Copyright 2017, Nature Publishing Group. Selenidostannates,[30] reproduced with permission from ref. 30. Copyright 2018, Royal Society of Chemistry. Iron oxide,[27] reproduced with permission from ref. 27. Copyright 2021, Royal Society of Chemistry, $BiVO_4$ with Bi vacancies,[31] reproduced with permission from ref. 31. Copyright 2022, Wiley-VCH.

As the field advances, a critical focus will be on understanding the fundamental mechanisms underlying materials synthesis within DESs.[26,27] These mechanisms enable researchers to not only harness the current capabilities more effectively but also to design novel DESs tailored specifically for unique materials synthesis challenges. The marriage of green chemistry principles, meticulous engineering, and innovative materials design is poised to reshape industries and technologies in ways that are sustainable, efficient, and at the forefront of scientific innovation. This review aims to summarize the application of DESs in the materials preparation process, starting from their unique and significant properties, combined with specific examples to propose how to design solvent systems according to various demands and purposes. At the end of the article, the authors also put forward the prospects for DESs in the materials preparation process.

2. Mechanisms and properties

2.1. Coulomb interactions and hydrogen bonding

The interaction form in DESs is quite complex because of the diversity of their single components. However, the main interactions are Coulomb interaction and hydrogen bonding interaction, and even multiple interaction modes. Despite some controversy, these non-covalent interactions are generally believed to be the cause of the lower melting point of the system. Hammond *et al.* studied a series of lanthanide nitrate hydrate-based DESs.[32] Due to the excessive number of species in the liquid mixtures, the observed nanostructures of intercalated hydrogen bonds containing water and urea were considered as a special structure, the lubricating molecular pseudophase. This bipartite structure observation helps explain some unusual physical properties, such as low viscosity and

high surface tension in type IV DESs. In another work, Ce^{3+} showed a different structure in the choline chloride and urea system from the above system.[22] The intermolecular coordination number shows that chloride ions dominate the cerium ligands. The coordination ability of urea is enhanced, while the coordination ability of nitrate is weakened. The results show that the choline chloride (in reline) significantly changes the environment around cerium ions, which further determines the kinetics of their hydrolysis process.

Similarly, urea can coordinate chlorides with strong hydrogen bonds. This forms a complementary choline shell around urea and chloride. In this way, due to the smaller spatial volume of the urea molecule, the binding probability is increased. In short, the results showed that reline has a strong and complex hydrogen bond network between species, which is consistent with previous NMR results.[33] A cage structure was proposed to illustrate the hydrogen bond interactions of various strengths in the DES. The same complex hydrogen bonding networks were also reported in others' work.[34,35]

To compare with the above work, Holbrey *et al.* conducted a series of neutron diffraction work on DESs under 338 K.[36] The results from EPSR showed that the generated model is consistent with the experimental data at these moderately elevated temperatures. In reline, the role of choline's hydroxyl group as a hydrogen bond donor or acceptor is less important than previously reported at 303 K. The same hydrogen bond network also exists in other types of DES. In some DESs containing alcohols (especially polyols), this phenomenon may be particularly noticeable.[37,38] Additionally, studies have shown that the structural network of glyceline is completely determined by its single content, glycerol, although the viscosity between the two is very different.[39] The network dynamics in glyceline are defined by the glycerol–glycerol dynamic correlation, which may be due to the poly-hydroxyl structure of glycerol. In contrast, the choline–glycerol dynamic correlation function in glyceline shows largely uncorrelated fluctuations. These findings indicate that glyceline is actually a highly correlated hydrogen bond network of glycerol molecules, similar to the choline chloride–urea system. The difference is that the choline ion in glyceline occupies the interstitial space and has almost no structural or dynamic correlation with the glycerol network. Therefore, the local transport and kinetic properties of glyceline are determined by relatively loosely bound choline ions because they dominate the structure and collective dynamics of glyceline. A comprehensive study based on ethylene glycol–DES (ethaline) has also reached similar conclusions.[40]

The hydrogen bonding supramolecular structure of a DES can be studied by DFT calculations, and the orientation of HBD and HBA can be well visualized.[41] A variety of information including electrostatic interactions, heat of formation, charge mobility, interaction energy, electron energy, zero-point energy, dipole moment, heat capacity, entropy, bond angles and dihedral angles can be provided. Among them, parameters such as bond length, bond angle, dipole moment and molecular energy play an important reference role. These properties mainly depend on the concentration of electron density to form nucleophilic sites, while electrophilic sites allow us to understand the properties that lead to physical and chemical phenomena. In addition, DFT calculations are often combined with molecular dynamics simulations to study the structural properties of DES.

When the HBD changes to a more polar carboxylic acid, a special structure, called "ionic domain", will form in the bulk of the DES.[42] In the malic acid–choline chloride system, the synergistic effect of them clamps the chloride anion through hydrogen bonding and electrostatic interaction, and then forms an ion cluster that is composited with the eutectic stoichiometry. This has been seen before in urea-based DES reline. However, the malic acid molecules with richer hydrogen bonding functionality (both hydrogen bonding donor and acceptor abilities) yield a 1 : 1 eutectic. It further showed the malic acid-based DES is more resilient to dissociation into clusters of the HBD molecules than is seen in reline. This structure is stabilized to a certain extent by the hydrogen bond interaction between HBD and choline molecules. This charge delocalization cage is surrounded by 6–7 other such cages, which is very similar to the radial structure of ionic liquids forming variable charges. This provides a basis for the extension of the related structure and properties of ionic liquids to DESs. Understanding these interaction modes and structures of components in DESs is vitally significant for the crystal nucleation when designing and preparing materials.

2.2. Polarity and acidity

The solubility of solvents is widely believed to be related to their polarity, where the principle of similar compatibility (like dissolves like) is the proof. In addition to the solvation process, dissolution sometimes involves chemical reactions, for example, in the case of calcium carbonate dissolved in hydrochloric acid. The capability to dissolve many substances (various precursors) is a prerequisite for the synthesis process in these green solvents. DESs are believed to have excellent dissolving properties. There is even research on the solvation of nanoparticles in DESs, which shows their excellent solvation properties.[43] Generally, there are two types of dissolution processes. One does not destroy the structural unit of the substance itself. The other completely dissociates substances into corresponding ions. Solutes in the former process are mostly molecular compounds, such as some natural products; the latter are mostly ionic compounds, such as metal oxides.[44–47] It is worth noting that in some dissolution processes, the formation of small molecules (such as water) is also involved. Therefore, the polarity of a DES largely determines the scope of substances to be dissolved.

Although they are considered to be substitutes for volatile organic solvents and have great potential in various applications, detailed knowledge of the dipolarity afforded by DESs was lacking before 2014. Understanding the polarity of DESs is essential if they are to be used as green alternatives to various volatile organic compounds in industry and academia. In terms of composition, conventional DESs are composed of molecular compounds (*i.e.*, urea) and ionic compounds (*i.e.*,

choline chloride). Therefore, the polarity of DESs should be higher than that of ordinary polar solvents and similar to the polarity of ionic liquids, which is why they are called ionic liquid analogues. So, how polar are DESs? Pandey and co-workers explored the behaviour of well-established solvent polarity probes dissolved in four choline chloride-based DESs.[48] Fluorescence dye maxima of emission and excitation along with the Stokes shifts in chosen DESs and several other common and popular solvents are compared. Normalized dipolarity can be determined by eqn (1) and (2),[48]

$$E_T(30) = 0.9953(\pm 0.0287) \times E_T(33) - 8.1132(\pm 1.6546) \quad (1)$$

$$E_T{}^N = \frac{\left[E_T(30)_{SOLVENT} - E_T(30)_{TMS}\right]}{\left[E_T(30)_{WATER} - E_T(30)_{TMS}\right]} \quad (2)$$

where $E_T(30)$ is dye betaine 30 (2,6-diphenyl-4-(2,4,6-triphenylpyridin-1-ium-1-yl)phenol), E_T^N is easier to determine as it is dimensionless and varies between 0 for tetramethylsilane (extremely non-polar) and 1 for water (extremely polar). The dipolarity of choline chloride-based DESs as reported using dye betaine 33 (2,4,6-triphenyl-1-(3,4,5-trichlorophenyl)pyridin-1-ium) was found to be significantly higher than even those of short chain alcohols. Results showed that the molecular structure of HBD in a DES plays a dominant role in dipolarity afforded by the DES, which is consistent with the experimental results of other tests.[39,49] The outcomes of Pandey's investigation work opened new avenues and laid the foundation for other research on the polarity of DESs.

Such solvation properties of DESs are believed to be difficult to define precisely and impossible to express quantitatively, whereas Kamlet–Taft solvatochromic parameters gained popularity later. Among them, α represents the hydrogen bond donor ability, β represents the hydrogen bond acceptor ability, and π* (determined by the shift of the absorption band of different probes) represents the polarity of solvents.[50] Marrucho *et al.* studied the polarity of different families of DESs by using solvatochromic responses of UV-vis absorption probes.[51] The results were similar to those obtained by normalized polarity.[48] HBA dominates the polarity of DESs, while the hydrogen bonding basicity in their studied DESs does not vary much within the same HBA. Further results showed that the DES displays a high capacity to donate and accept protons when compared with common solvents (including ILs). They concluded that the polarity of DESs can be easily designed by choosing their single components.

In addition to optical spectroscopy, chromatography is also a good method for studying molecular interactions in DESs. Such method has been proved to perform well in solvents such as ionic liquids, so it has been extended to the field of eutectic systems.[52] Anderson *et al.* conducted the first study to measure chromatographically solute–solvent interactions of some carboxylic acid-based DESs.

$$\log SP = \log K = c + eE + sS + aA + bB + lL \quad (3)$$

where the dependent variable log SP refers to some property of a series of solutes in a fixed phase (or phases). For example, SP could be L, the gas–liquid partition coefficient for a series of solutes in a given liquid.[53] Thus in eqn (3), k refers to the retention factor of each probe molecule for the DES stationary phase at a specific temperature. The retention factor is calculated chromatographically by measuring the retention time of each solute as well as the column dead volume. Factors represented by capital letters (E, S, A, B, and L) are solute descriptors: E, excess molar refraction calculated from the solute's refractive index; S, solute dipolarity/polarizability; A, solute hydrogen bond acidity; B, solute hydrogen bond basicity; and in Anderson's work, and L is solute gas–hexadecane partition coefficient at 298 K.[50] Retention factors and solute descriptors are used to measure the system constants (e, s, a, b, l) that characterize the multiple solvation interactions of the solvent: e is the ability of the solvent to interact with π- and n-electron pairs of the solute; s describes the dipolarity/polarizability of the solvent; a is the measure of the hydrogen bond basicity; b is the hydrogen bond acidity; and l describes the difference between the hydrophobicity or lipophilicity of the two phases.[50,53]

It was found that DESs composed of larger molar ratios of low pK_a HBAs result in systems with higher hydrogen bond acidity. Further optical spectroscopy experiments showed that an increase in temperature led to reduced acidity of HBDs in choline chloride-based DESs.[54] However, the dipolarity/polarizability and the basicity of HBAs did not change with the temperature of DES.

Some nuclear magnetic resonance probes (such as pyridin-*N*-oxide) can also be used to determine the solvatochromic parameters of DESs.[55] The understood strong intrinsic interaction (hydrogen bonding interaction) determined by these solvation studies can be used to interpret the excellent extraction performance of DESs. More importantly, it makes it possible to predict and understand the dissolving properties of DESs, and finally, guide the synthesis of task-specific solvents.

Some other properties of DES are determined by polarity as well. Jackson *et al.* investigated the structures of proteins in a DES and its water mixtures by circular dichroism and small-angle neutron scattering.[56] Based on the results of protein conformation in the DES, they put forward a hypothesis: the conformation of protein depends on the solvation environment of amino acids that promote protein folding, and these amino acids are likely to be responsible for their enzymatic activity. In DESs, HBDs replace the water surrounding the amino acid in the active site, which promotes a partially folded conformation and reduces activity through a combination of specific binding and reduced solvophobic effect. In addition, in the case of hydrated DESs, water may form a shell around these active sites, allowing the protein to fold in the buffer. The solvated electron has also been observed in DES, and this provides the possibility of enzyme-catalyzed reactions in DESs.[57]

According to a publication by Milano *et al.*, the photosynthetic reaction center of bacteria (*Rhodobacter sphaeroides*) in DESs can generate a charge-separation state and even perform

its natural light cycle.[58] This discovery not only verified the good maintenance of the protein structure in DESs, but also implied that DESs possess excellent electron solvation and transport properties.[57] When considered for electrochemical applications, fast electron transfer in DESs is a strong advantage. Different types of solvent systems are critical to energy storage density. In Hapiot's work, the electron transfer rate constant measured in ethaline is close to that reported for the oxidation of ferrocene or ferrocyanide in water in an organic solvent.[59] This shows that from the point of view of electron transport rate, DES (at least ethaline) seems to be more similar to molecular solvents than ionic liquids. In addition, the report of ultra-stable free radicals in DESs illustrates their great potential applied in electrochromic devices.[60]

2.3. Heterogeneity and nanostructure of DESs

The permanent dipoles of polar solvents give them polarization ability, which tends to concentrate the charge of covalent bonds, or separates ionic compounds into solvated ions. The value of the dielectric constant (ability to separate charge) increases with the increase in the permanent dipole of the molecule. Given that HBDs are usually polyols, polyacids or amides, DESs theoretically belong to a class of protic solvents. However, the presence of ionic regions in DESs allows the local polarity to reach the level of ionic compounds. Therefore, they cannot be simply classified into any conventional solvent class.

Heterogeneous and amphiphilic nanostructures have been shown to play a pivotal role in ionic liquids, which had not been experimentally proved in DESs before 2017.[61] Through the application of some experimental techniques such as neutron diffraction and ultrafast spectroscopy, these properties were gradually unveiled.[62–65] In this way, DESs can be better utilized by designing the characteristics related to their nanostructures.

Kuroda *et al.* conducted a thorough investigation on a series of amide-based DESs, trying to find evidence of molecular heterogeneities in such systems.[66] In principle, the ultrafast kinetics is attributed to the formation and breaking of hydrogen bonds between amides. A slow dynamic component observed in the time evolution of the photon echo signal was considered to be related to the asymmetry and polarity of the HBA. Interestingly, it was found that the level of heterogeneity in apolar domains increased with the asymmetry in the geometry and the strength of interaction between HBA and HBD. Domains created by heterogeneity slowed the formation and breakage of hydrogen bonding interactions, thereby rationalizing the overall dynamics.

Neutron diffraction has proved to be an effective technique for studying the molecular-level structure of a liquid system. The experiment conducted by Atkin *et al.* revealed the phenomenon of cationic alkyl chain association in DESs.[67] As the chain length increases, this association becomes stronger, indicating the higher the degree of amphiphilicity of DESs. Understanding this amphiphilic ability contributes to the design of DESs, and to dissolving more diverse solutes.

In addition, some ingenious experimental methods from ionic liquids have been carried out in DESs, which benefits the study of their spatial heterogeneity.[68] The electrostatic field can be estimated from infrared experiments based on the Stark effect, which can be used as an effective method to illustrate the microscopic heterogeneous solvation of DESs. Bagchi *et al.* investigated four choline chloride-based DESs (the HBDs are diols with different lengths of alkyl chains).[69] The results showed that the total electrostatic field can be decomposed into contributions from HBA and HBD constituents to obtain an in-depth understanding of the nanoscale heterogeneity of the DESs around the solute molecule. Compared with neutron scattering and ultrafast spectroscopy, infrared spectroscopy experiments are easy to operate, and the results can also be supported by molecular dynamics simulations.

Hydrophobic DESs have received widespread attention since their proposal. The most typical example of these novel DESs is DL-menthol and lauric acid. Kashyap *et al.* performed atomic and molecular dynamics simulations to understand the bulk phase morphology that is present in the hydrophobic eutectic solvent based on DL-menthol.[70] The pre-peak in simulated total X-ray scattering structure function indicated the presence of intermediate-range structural heterogeneity in the studied hydrophobic DESs. This further indicated the existence of polar regions composed of only polar groups, and these domains were distributed in a non-polar environment formed by the non-polar groups of DL-menthol and the alkyl tail of the HBD. That is to say, the reason for the hydrophobicity of these DESs is that the intrinsic "huge" non-polar regions hinder the interaction between the polar regions and water, thereby hindering the solvation process. In addition, the results of real-space correlations and angular-resolved radial distribution function indicated that the structures of these DESs were dominated by strong hydrogen bonding interactions between all species. All these balance correlations control the overall stability of the DES, thus hindering the crystallization of the system. This is consistent with the results from neutron diffraction.[23,71] In addition, studies have shown that there is also time heterogeneity in DESs, which is still significant even at temperatures 100–160 K higher than their glass transition temperatures.[72,73]

Before 2017, although there were some comprehensive studies on the ontological properties of DESs, there was almost no research on their structure and properties at the interface. Understanding the behaviour of these solvents on the energized interface will facilitate their application in electrochemistry. Kaur *et al.* applied all-atom molecular dynamics simulations to explore the morphology and nanostructure of reline in bulk and interfaces.[74] Studies have shown that urea molecules exhibit different orientations near the positively charged and negatively charged electrodes, which may be related to the carbonyl group (π electrons) in urea. There is a significant short-range interaction between the neutral graphene electrode and choline in reline. The existence of the multilayer structure of the reline near the charged electrode is also reflected in the electrostatic potential and electric

field distribution. More importantly, the calculated differential capacitance reveals the dependence of electrostatic properties on the shape and size that molecules exhibit near the electrodes. Within a year, a similar work was reported. The results of De Proft *et al.* further indicated that the distinct orientation of urea in the electric double layer is determined by the charge on the surface.[75] The difference of ±0.32 C m^{-2} on the electrified surface causes a 90° rotation of urea. These results provided new insights into the electric double layer structure of DESs, whose interface structure can be adjusted and designed at the molecular level.

Fig. 2 shows two pioneering works illustrating the heterogeneity of DESs. Conducted by Kaur and colleagues, the simulation efforts encompassed a molecular dynamics study investigating the X-ray and neutron scattering structure of DES (acetamide + $LiClO_4$, molar ratio = 81 : 19).[61] Fig. 2a reveals that the studied DESs exhibit distinct spatial heterogeneity at the molecular length scale. The result clearly indicated that both $LiClO_4$–$LiClO_4$ correlations and the $RCONH_2$–$RCONH_2$ term significantly influence the pre-peak phenomenon, underlining the substantial role played by potent electrostatic interactions in shaping the structural characteristics of these systems. Conversely, the principal peak predominantly stems from the self-correlations of $RCONH_2$. However, both $LiClO_4$–$LiClO_4$ and $RCONH_2$–$LiClO_4$ contributions moderately impact the principal peak. The accompanying figure illustrates the consistent nature of the electrolyte's influence on the pre-peak, irrespective of variations in alkylamide tail length. Similarly, the alkylamide contribution remains unaltered despite tail modifications. The nanoscale-sized extended domains of $LiClO_4$ (highlighted in red) are readily discernible within the equilibrium snapshots of the depicted DES in Fig. 2b. The system exhibits pronounced heterogeneity, marked by the uneven distribution of alkylamide molecules and ions. Since then, a number of articles investigating microscopic heterogeneity have emerged.

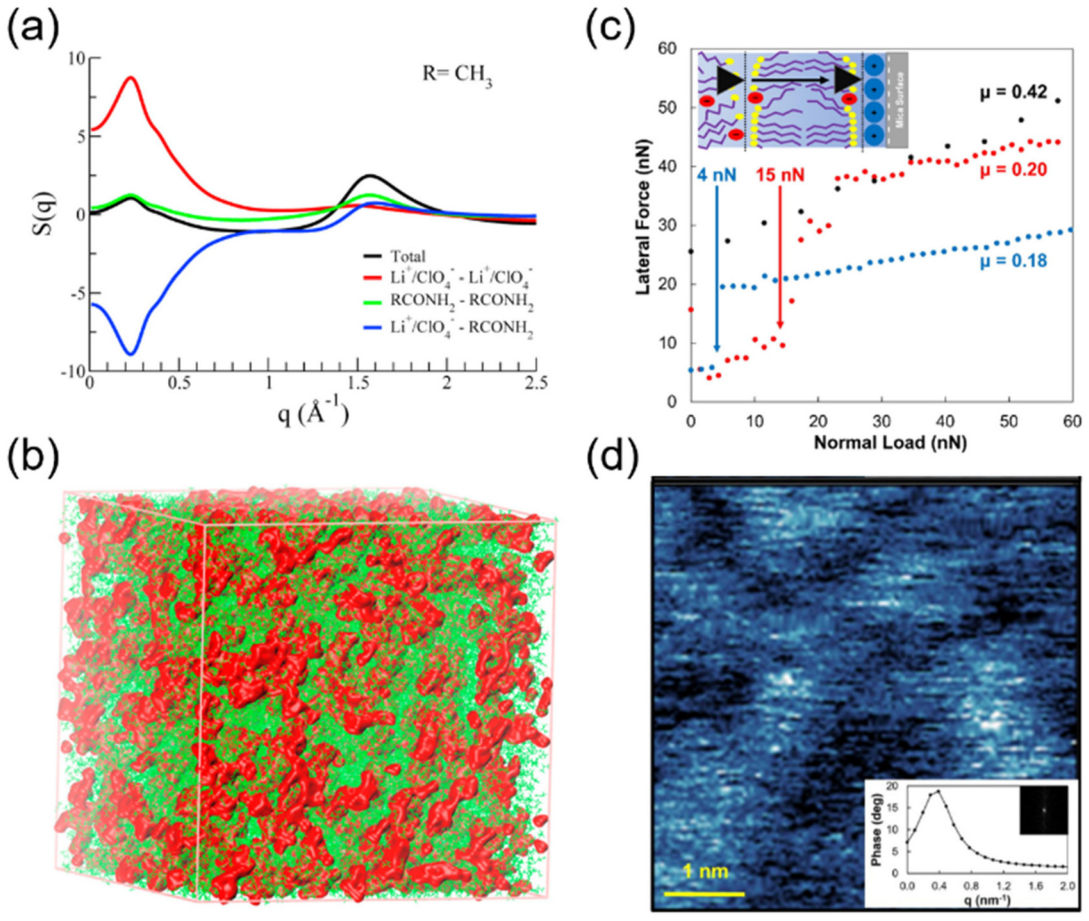

Fig. 2 Simulation and experiment investigation of heterogeneity in DESs. (a) Partial X-ray scattering S(q) for DES (acetamide + $LiClO_4$). (b) Equilibrium snapshots of the DES (the Li^+/ClO_4^- ion pairs are shown as a red isosurface in all of the systems, while the acetamide molecules are shown in green).[61] Reproduced with permission from ref. 61. Copyright 2016, American Chemical Society. (c) Lateral force *vs.* normal force of mica in air (black), ChCl/BuOOH (blue), and ChCl/HeOOH (red). The friction coefficient (*m*) is derived from the slope of the boundary regime. The inset illustrates a representative schematic depicting the shift from the multilayer regime to the boundary regime when considering ChCl/HeOOH on mica. (d) 5 nm by 5 nm AM–AFM phase image of mica immersed in ChCl/HeOOH. Insert: the 2D fast Fourier transform image and radial average value.[76] Reproduced with permission from ref. 76. Copyright 2022 Elsevier.

In Buzolic's work, the structure of DESs formed by mixing ChCl with butyric acid (ChCl–BuOOH) and hexanoic acid (ChCl/HeOOH) at a molar ratio of 1 : 4 was studied, attempting to investigate the effect of carbon chain length on heterogeneity.[76] With the aliphatic chain increases from C4 to C6, the nanostructure becomes larger and more defined, and the AFM force curves show that the interfacial nanostructures extend farther from the surface (Fig. 2c and d). The AFM force curves depict an expansion of the interfacial nanostructures away from the surface. The self-assembled nanostructures in these systems emerge from the convergence of choline cations, chloride anions, and acid-alcohol groups, yielding polar domains through electrostatic attraction and hydrogen bonding. Within this context, alkyl chains endowed with carboxylic groups are effectively excluded from polar domains, congregating instead within nonpolar domains.

The phase behaviour of both bulk and confined DESs was also investigated. Gardas *et al.* used non-ionic surfactant (Tween-80) and cyclohexane to study the reverse micellar system based on DES (benzyltripropylammonium chloride : ethylene = 1 : 3).[77] All the vibrational modes of HBA were found to be significantly red-shifted in the DES compared with pure substance, which indicated the strong intermolecular association between HBAs and HBDs during the formation of the eutectic system. Laman spectra indicated a disruption of hydrogen bonding interactions between HBAs and HBDs when forming a reverse micellar system. In another work, the phase behaviours of both bulk and confined DESs in controlled pore glasses were also investigated.[78] Lan *et al.* conducted a thorough test on the thermodynamic properties of reline, the most typical DES. Differential scanning calorimetry revealed that under nanoconfinement, the melting points and enthalpies are reduced, while the cold crystallization temperatures become higher. A new crystal structure of reline in the 50 nm pores was proved by X-ray diffraction analysis. Similar to the reverse micellar result, the thermodynamic and kinetic properties of reline manifested the significant role played by the hydrogen bonding interactions when forming the eutectic system. Understanding the structures and thermodynamic properties of DESs beyond their bulk lays the foundation for expanding their new applications.

Quaternary ammonium salts such as choline chloride are usually used as HBA to construct DESs. The length of the aliphatic chain not only affects the melting point and other properties of the system, but also determines the solvent kinetics of DESs. One of the reasons why ionic liquids are liquid at room temperature is that their asymmetric structure hinders the crystallization process. As the analogues of ionic liquids, do DESs follow similar laws? Samanta *et al.* investigated the liquid structure of different DESs (HBAs with various chain lengths) by monitoring the fluorescence response of probe molecules.[79] The results indicated that the spatial and dynamic heterogeneity in DESs were more pronounced with longer alkyl chains, which was consistent with the recently reported results.[80] The translational and rotational diffusion dynamics of selected probe molecules indicated that heterogeneity arises through the formation of molecular-scale domains, which becomes more pronounced in solvents with longer chain lengths.

Similarly, several works exploring the effect of alkyl chains in HBD were also reported. Bagchi *et al.* conducted 2-dimensional IR spectroscopy research on three DESs (HBAs are 1,2-ethanediol, 1,3-propanediol, and 1,4-butanediol).[81] The result showed that as the length of the hydrocarbon chain increases, a reasonable reason for the slower solvent kinetics is the difference in viscosity of the DES. The fast component in the solvation kinetics was attributed to the fluctuation of the solvent in the first solvation shell, whereas the centre of mass of the molecule did not change significantly. Therefore, the time scale of the diffusion motion depends on the DES viscosity, which is consistent with what Samanta *et al.* reported.[79] In another work, Samanta and Hossain studied the kinetics of hydroxyl localization (on HBD) on their diffusion.[80] Compared with the length of the alkyl chain, the spatial and dynamic heterogeneity changes with the position of the hydroxyl group are insignificant.

Vis *et al.* developed a statistical model combining theoretical and experimental results to predict the non-ideal behavior of eutectic mixtures.[82] Studies have shown the existence of a strong correlation between the non-ideality of the system and the volume of the quaternary ammonium salt, and smaller ionic bonds will lead to stronger interactions. Due to the shorter side chain the distance between N^+ and Br^- is reduced, and Br^- will experience a stronger interaction than the –OH of carboxylic acid or polyol. Understanding the solvation properties and solvent dynamics of DESs is conducive to designing task-specific solvent systems for various applications. Knowing the interaction between components at the molecular level lays the foundation for the synthesis of molecules and materials in DESs.

2.4. Stability and reactivity

The relatively high thermal stability of DESs is of great value because it directly affects the sustainable application of these solvents at high temperature and the stability of the materials synthesis processes. High temperature is necessary in many synthetic reactions and industrial applications, so the thermal stability of DESs is crucial to ensure the efficiency and quality of synthesis.

On the one hand, the thermal stability of DESs is related to their reliability as reaction media. Some separation and synthesis processes need to be performed at relatively high temperatures to achieve the desired product conversions and selectivities.[83,84] If DESs decompose at undesired temperatures, it will lead to reaction failure or product with low purity. Therefore, DESs need to be stable at high temperature to ensure the smooth progress of the reaction. On the other hand, thermal stability is crucial for the control of materials synthesis. The preparation of many advanced materials requires high-temperature conditions to achieve the desired crystal growth, phase transition or other physicochemical changes. If DESs decompose during the synthesis process, it

may affect the structure and properties of the material, and even lead to unpredictable results. Therefore, the use of DESs with good thermal stability during materials preparation helps to ensure the consistency and controllability of the synthesized materials.

Chen *et al.* studied the thermal stability of 40 DESs and found that the thermal stability of HBD has a crucial influence on the T_{onset} of the system.[85] In general, the DES will first break down into HBD and HBA because of the weakness of hydrogen bonding interactions at high temperature. Subsequently, HBD, which is less stable, starts to volatilize or decompose; HBA also volatilizes or decomposes, but at a higher temperature. Hydrogen bonding plays an important role in the thermal stability of the DES, and it hinders the "escape" of molecules, so that it requires greater energy to decompose than pure HBA and HBD, which causes the T_{onset} of the DES to shift to a higher temperature. For the first time, Janković *et al.* presented the physicochemical elucidation of the overall thermal decomposition mechanism and the effect of enthalpy–entropy compensation on the emerging reaction mechanism for investigating type II DES ($MgCl_2{\cdot}6H_2O:ChCl$).[86] It was found that the thermodynamic principle of the enthalpy–entropy compensation is the source of the kinetic compensation effect, which is the consequence of the molecular interaction effect during the thermal decomposition of type II DES. The key phenomenon in the complex multi-step process is the parallel dehydration steps of $MgCl_2{\cdot}6H_2O$ in DES, corresponding to the above work by Chen and coworkers.

For some DESs containing carboxylic acids (especially dicarboxylic acids), the decomposition temperature is even lower than the preparation temperature of the DES.[87] This puts forward new requirements for the preparation method of the DES, and the grinding method and ultrasonic method came into being. Although many impressive results have been obtained, research on thermal stability has not stopped. High-resolution TGA experiments were performed by Liu *et al.* which provide a clearer view than both the slow and fast heating rate in conventional TGA.[88] The long-term thermal stability of DESs was also investigated.[89]

Electrochemical stability is very significant as well. The electrochemical stability of solvents, especially those with broad electrochemical windows, is of great significance in practical production and wide applications. The electrochemical window refers to the potential range in which electrochemical reactions can be performed in a solution, and a wide electrochemical window is beneficial for:

1. Realizing multiple reactions in the same system
2. Improving the control and stability of the reaction
3. Providing a wider working potential range.

Li *et al.* investigated the electrochemical potential window of 24 choline-based DESs, and the choline–methyl urea system has the largest value, which is 4.72 V.[91] The broad electrochemical window of DESs makes their application in electrochemistry more diverse and flexible. It not only promotes the integration of various electrochemical reactions, but also provides support for high efficiency, stability and innovation in actual production, and promotes technological development in the field of materials preparation. In addition, the radiation stability of DESs was investigated, as was the study of ionic liquids.[92,93] There are also some publications about the corrosivity of DESs to containers or electrodes, which is very important.[94]

2.5. Effect of temperature and water content

The influence of temperature on the properties of solvents is huge. For example, it will change the viscosity and then change some transport properties. Temperature also has a great influence on the intrinsic polarity and internal noncovalent interactions of DESs. It was reported that an increase in temperature leads to reduced acidity of HBDs in choline chloride-based DESs.[95] However, due to various reasons, such as the instability of the probe in a DES, it seems difficult to achieve a unified result on polarity parameters of DESs.[54] Unlike the polarity parameter (which contains many parameters), the result of heterogeneity is relatively straightforward. Kashyap *et al.* explored the molecular-level structures of DESs and the variation with temperature by molecular dynamics simulation on X-ray scattering and neutron diffraction.[61,90] The result showed that increasing temperature leads to the increase of nanoscale heterogeneity because of ion-pair segregation in the studied DESs. In the X-ray scattering results (Fig. 3a), the left peak in a curve, called pre-peak or first sharp diffraction peak, represents nanoscale structural organization, and corresponds to self-segregated domains of Li^+/ClO_4^-. The results of radial distribution function (Fig. 3b and c) show that whether it is ions of the same charge or ions of different charges, as the temperature increases, the nearest neighbouring peak is slightly shorter. In addition, as the temperature increases, the height of the peak increases significantly, which means stronger ion pairing and ion-pair segregation at higher temperatures. In the acetamide/lithium perchlorate system, the molecular-ion behaviour is exactly the opposite (Fig. 3d). In short, increasing temperature led to the increase of nanoscale heterogeneity because of the ion-pair segregation in the studied DESs.

Similarly, the hydrophobicity of DES also changes with temperature. Longeras *et al.* reported a thermal-switchable smart DES.[96] When the temperature of the system is higher than 26 °C, the original DES–water system will separate to two phase. In other words, the hydrophilicity of DES decreases with increasing temperature. Considering that both ammonium and oleate ions are more soluble than their neutral form in water, this phase separation phenomenon was believed to be induced by a decrease in ionicity. It is worth mentioning that the value of the DES–H_2O system lies not only in the regulation of viscosity and polarity, but also in reducing the cost of solvents used for synthesis.

3. Solvothermal method

The solvothermal method based on DESs is not limited by water, achieving a wider range of chemical environments,

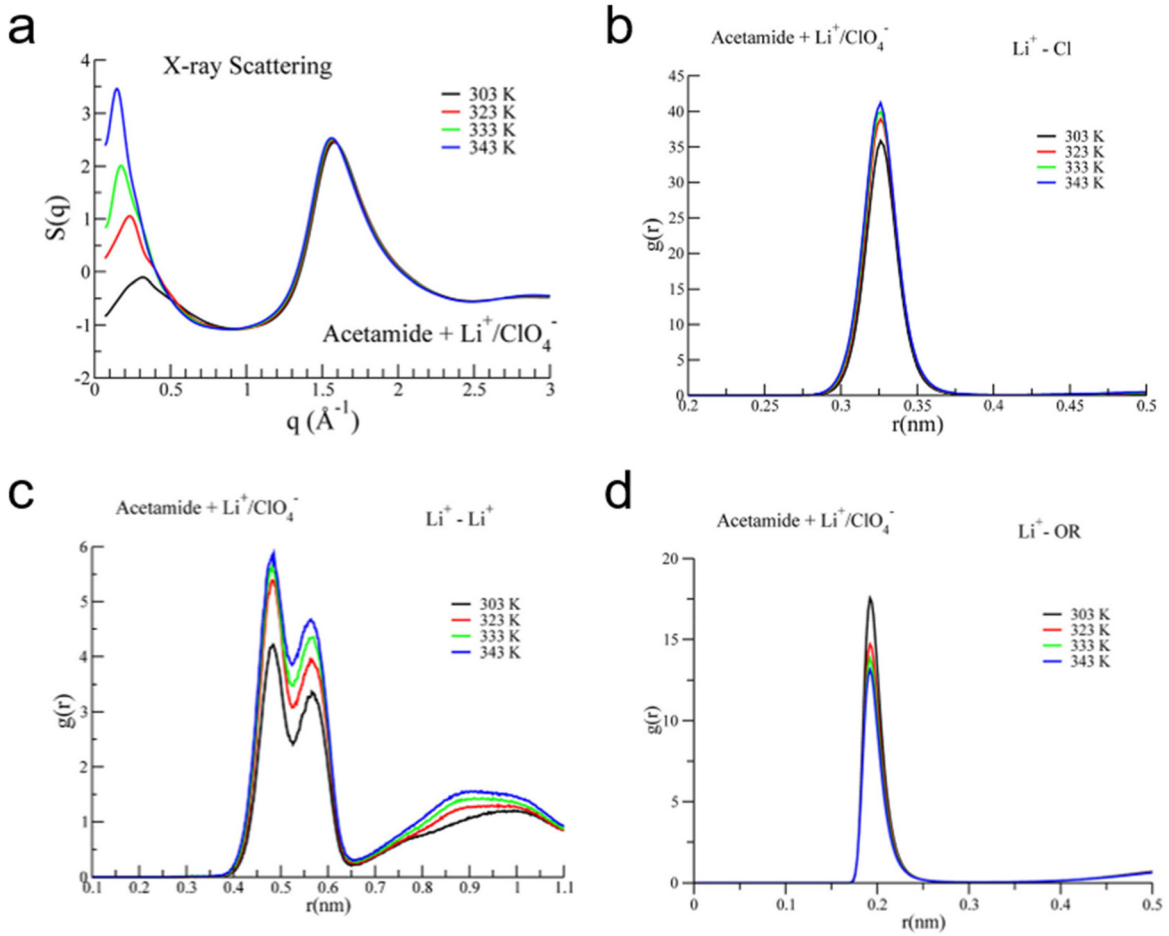

Fig. 3 (a) Temperature dependence of X-ray scattering structure functions for acetamide + Li^+/ClO_4^-. Temperature-dependent radial distribution functions for (b) Li^+–Cl, (c) Li^+–Li^+, and (d) Li^+–OR. OR is the oxygen atom in acetamide, and Cl is in ClO_4^-.[90] Reproduced with permission from ref. 90. Copyright 2018, American Chemical Society.

which is helpful for the synthesis of different materials. For example, product crystal structure and morphology can be controlled at higher temperatures and pressures. In addition, DESs are generally considered to have good solubility and miscibility, which facilitates dissolving the reactants, thereby enabling processes that cannot be carried out in aqueous systems.

3.1. Metal organic frameworks

In 2009, Zhang and coworkers reported the structure-directing roles of DESs, followed by investigating their performance in gas capture.[20] As shown in Fig. 4, the first role observed in compound **1** is the introduction of cations and anions. In **1**, the cationic choline ion acts as the extra framework structural directing agents (SDAs), while the chloride ion binds to the polymer layer. The second role was observed in the three isomorphic compounds, in which the chloride ions are the extra framework SDAs. The neutral urea molecule is bonded to the framework. The third effect observed in compound **3** is opposite to the second one, because choline ions bind to the framework through their hydroxyl groups, and the molecule acts as an SDA outside the framework. Finally, the fourth role observed in compounds **4–6** is the direct binding of neutral molecules to the polymer backbone. TGA showed the main structure of selected MOF (compound **6**) possesses a pretty high thermal stability (almost 0 weight loss up to 550 °C), and the N_2 adsorption/desorption study revealed its microporous structure. Further tests showed the BET and Langmuir surface areas are 186.3 and 261.5 $m^2\ g^{-1}$, respectively. Since 2006, many synthetic paradigms and methodological works have been reported in the development of synthesizing framework compounds in DESs.[29,97,98]

3.2. Nanoparticles

It has been demonstrated that the choice of solvents used to synthesize nanoparticles can affect their surface chemical composition, morphology, and fluorescence characteristics. Genç *et al.* used a multiple-solvent system to prepare hydrophilic and hydrophobic carbon dots through solvothermal synthesis.[99] In this method, carbon dots were prepared in a DES, while the traditional solvent system was used for separation. The waste products of centrifugation can be minimized, and

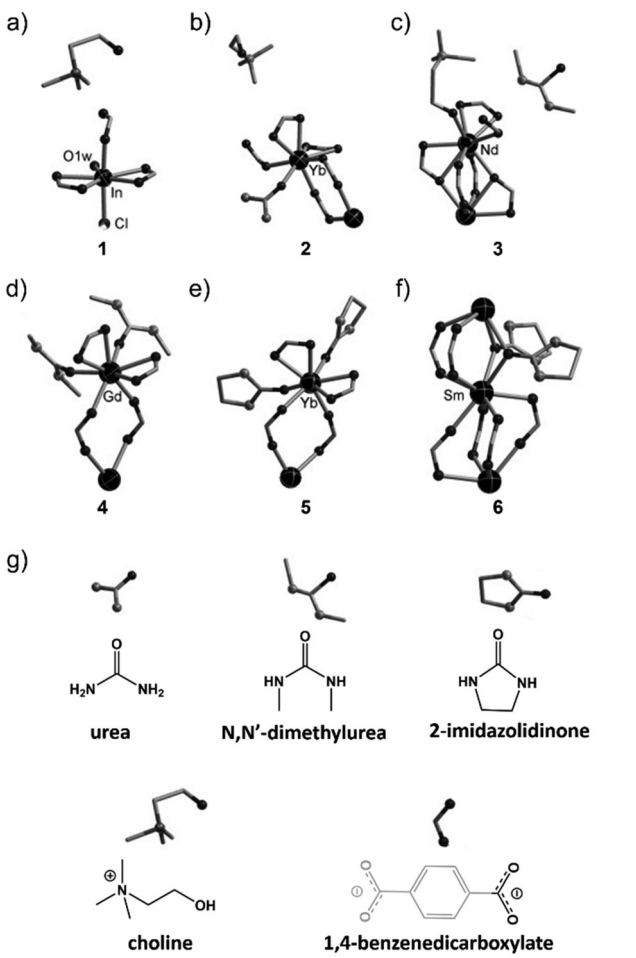

Fig. 4 The coordination shell of the metal central and the guest component in (a) **1**, (b) **2**, (c) **3**, (d) **4**, (e) **5**, (f) **6**, where O is in black, N is in gray, and O_{1w} represents water oxygen atom. (g) Chemical structure of different ligands.[20] Reproduced with permission from ref. 20. Copyright 2009, Wiley-VCH.

the particle recovery rate was increased by 90%. Moreover, the photoluminescence and electronic characteristics of the synthesized carbon dots were adjustable. The hydrophobic and hydrophilic carbon dots reported here can be used in functional textiles, electronic products, and biomedical imaging.

Nitrogen fixation is an important reaction that causes significant energy consumption every year. Therefore, it is very valuable to find catalysts with low cost and high efficiency. Electrocatalysis of nitrogen to ammonia at ambient temperature is a desired way for tackling the issue. Zhao and coworkers reported the DES-solvothermal synthesis of nanostructured Fe_3S_4 *via* a one-pot reaction.[100] The obtained Fe_3S_4 catalyst exhibits high NH_3 yield (75.4 μg h^{-1} mg^{-1} cat.) and faradaic efficiency (6.45%) at −0.4 V *vs.* reversible hydrogen electrode.

Synthesizing other particles with adjustable size in DESs is also possible. Jiang *et al.* reported for the first time the use of PEGylated DES for the solvothermal synthesis of nickel–cobalt sulfide.[101] Compared with the traditional vulcanization route, this route is cost-effective and energy-efficient, combining solvothermal synthesis and vulcanization processes. The structure and composition of the synthesized sulfide can be adjusted by adjusting the ratio of the reactants. PEGylated DES was believed to play multiple roles, including as a solvent, shape control agent and sulfur source in the synthesis of sulfides. The prepared sulfide exhibited excellent oxygen evolution reaction performance, almost no deactivation after 2000 cycles, while the Faraday efficiency was higher than 95%. This research provides a new method for synthesizing layered-structured metal sulfides for energy conversion and storage applications. Torrente-Murciano *et al.* proposed a new method for preparing V_2O_5 with different morphologies using a DES (reline).[102] This work overcame the dependence of current synthesis methods on shape-directing agents (such as surfactants). Selective formation of V_2O_5 3D beads, 2D nanosheets and 1D randomly arranged nanowires can be achieved by tuning the water content in reline. The results of electrospray ionization mass spectrometry proved the formation of alkylamine-based ionic species during the heating process, and these ionic species play a significant role in the resulting material morphology with template and exfoliation characteristics. The nanostructured V_2O_5 cathode showed a fast charge–discharge response, which makes it a potential electrode for batteries.

3.3. Composite materials

DESs have been used as green and sustainable media, acting as solvents and structure inducers when synthesizing composite nanomaterials. Pal *et al.* reported a facile approach for the fabrication of anisotropic bimetallic gold–copper nanostructures by using reline.[103] The precursor ($CuCl_2$) was found to impact the reduction kinetics of the reaction, and further affect the morphology and elemental composition of final product. The fabricated nanoparticles revealed a high SERS signal for crystal violet molecules adsorbed at their surfaces. Zhang *et al.* developed an electrochemical activation process to trigger a reversible phase change reaction and surface reconstruction to synthesize highly active and stable self-supporting Ag nanoparticles grown on a Cu substrate.[104] Activated Ag NPs/Cu have a larger surface area, more accessible active sites, and strong metal–support interaction with tailored atomic/electronic structure, thereby improving electrochemical catalytic activity. The electrode optimized by the subsequent ion-exchange method shows ORR performance equal to or better than that of the most advanced Pt/C and has excellent electrochemical stability and methanol tolerance.

Fu *et al.* reported the use of DES (ethaline) to synthesize tungsten oxide–molybdenum oxide composite materials.[105] The synthesized material is composed of agglomerated particles, and the crystal size ranges from ~56.0 nm to ~68.0 nm, depending on the reaction temperature. UV-vis irradiation test showed the composite material possesses photochromic properties with good reversibility and cyclability. Compared with the conventional method of preparing metal oxides, the synthesis temperature of the above work is much lower.[106] In another work, a flower structure g-C_3N_4/BiOCl/$BiVO_4$ with a

ternary heterojunction was synthesized by a solvothermal method in DES.[107] The synthesized nanoflowers showed excellent catalyst stability and extraordinary durability on oxygen evolution reaction. Such ternary heterojunction was demonstrated to extend the life of the photogenerated charge, and improve the separation efficiency of photogenerated electron–hole pairs. The above work provides new insights into the design of catalysts using green solvents. Similarly, a Ni–Fe layered double hydroxide nanosheets/sulfur-doped graphite carbon nitride heterostructure can be prepared in DESs.[108] The combination of the layered structure provides a synergistic quantum confinement effect and promotes abundant active sites. The development of advanced architectures with lower energy requirements and minimal by-products signifies the superior characteristics of synthetic methods within the guidelines of green chemistry.

3.4. Specific structures

Gan *et al.* demonstrated an efficient method for preparing N/O self-doped hollow carbon nanorods from ternary DES.[110] The open hollow nanorod structure provides high capacity and long-term cycling stability. Similarly, Pérez-García and co-workers reported a work in which hydrophobic DESs were used to synthesize polyacrylamide macroporous materials. The γ-Fe_2O_3 nanoparticles precipitated on the porous surface of high internal-phase emulsions, thereby providing the final materials with magnetic properties and electrostatic performance.[111] Dye adsorption experiments showed that the synthesized material has a strong adsorption capacity (>350 mg g^{-1}) and good recycling performance. This functional material is expected to be used for precision-controlled cleaning robots.

Materials with high surface area, abundant active sites, and enhanced electrical conductivity are highly desired for supercapacitors. Ding *et al.* reported a method of K cation-intercalated birnessite-type MnO_2 *via* a facile room-temperature wet-chemical process.[109] The DES used is a quaternary component system: monoethanolamine (MEA), diethanolamine, and triethanolamine are used as HBDs, and ChCl is used as HBA. During the preparation, K^+ can be pre-intercalated into the birnessite-type MnO_2 layer by adding ethanolamine-based DES (Fig. 5a). In addition, the morphology, crystallinity, and porosity of manganese oxides can be effectively tuned by changing the type of HBD in the DES (Fig. 5b–e). The as-prepared MnO_x material exhibited the best electrochemical performance, including high specific surface area (220 m^2 g^{-1}), high specific capacitance (290 F g^{-1}), and high stability (92.5% retention over 8000 cycles). In another work, a DES-assisted method of fabricating $BiVO_4$ photoanode with bismuth vacancies was proposed, which can significantly enhance the charge diffusion coefficient by 5.8 times, thereby enhancing the charge transport efficiency (Fig. 5f–k).[31] As is shown in Fig. 5f, the hydrogen bond network between ethylene glycol and choline chloride is the driving force in the preparation process. At the solid–liquid interface, the crystal lattice energy is weakened and Bi atoms are leached out by Cl^- ions. The charge transfer efficiency was further enhanced by loading the CoBi cocatalyst, achieving 4.5 mA cm^{-2} at 1.23 V compared with the reversible hydrogen electrode under AM 1.5 G illumination. The above work refines cation defect engineering to enable the same potential for charge transport properties of different types of semiconductor materials for solar fuel conversion.

As mentioned above, to some extent, the introduction of water does not change the structural properties of DESs.[112] However, transport properties such as viscosity vary significantly with water content. Some solvothermal reactions can be carried out in DES–water systems. Similar to "pure" DESs, hydrated DESs were believed to play a triple role (solvent, reactant and template) in synthesis processes. The added water in these eutectic systems is responsible for adjusting viscosity, pH, polarity, *etc*. In some research work, the precursors were first dissolved in water and then mixed with DESs for further reactions. In others, water was added to the mixture of the precursors and DESs. Wang *et al.* prepared slender $BiVO_4$ microtubes with a monoclinic structure on a large scale by the solvothermal method.[113] A certain amount of water was added to the solution to adjust the viscosity of Reline. The length of the $BiVO_4$ microtube is about 800 nm, and the wall thickness is about 100 nm. The openings of the synthesized microtubes exhibit a jagged structure. The formation mechanism of slender microtubules is attributed to complex collaboration, which involves the reaction-crystallization process controlled by BiOCl and the nucleation growth process of nanosheets induced by the reline–water system.

The rapid, controllable, and green synthesis of TiO_2 is still a challenge for its large-scale preparation and application. Tang *et al.* compared a series of TiO_2 prepared with different DES systems (Fig. 6).[114] The photocatalytic water-splitting performance of the prepared catalyst is 13.13 mmol h^{-1} g^{-1}, which is 18 times that of commercial P25 TiO_2. The higher activity is attributed to the *Crassula perforata*-like shape with surface heterojunctions and defects. This research provided a new way for a green and fast way for synthesizing other photocatalysts.

DESs sometimes participate in the reaction as a reducing agent, which may be because of the reductive activity of single components. A typical example is the DES which contains ethylene glycol. Karimi and Eshraghi reported a facile method for synthesizing Mn_3O_4 nanoparticles.[115] Microscopic elemental studies showed spherical nanoparticles with an average particle size of 25 nm. The magnetic characteristics of the synthesized Mn_3O_4 nanoparticles reveal their paramagnetic behavior at room temperature. In addition, manganese oxides with different element ratios and different morphologies can also be synthesized in the DES–water system.[116]

4. Electrodeposition method

Benefiting from a wide electrochemical window, DESs have many advantages in the electrodeposition process of metals, alloys, compounds and composite materials. For example, high potentials can be applied so that electrodeposition can

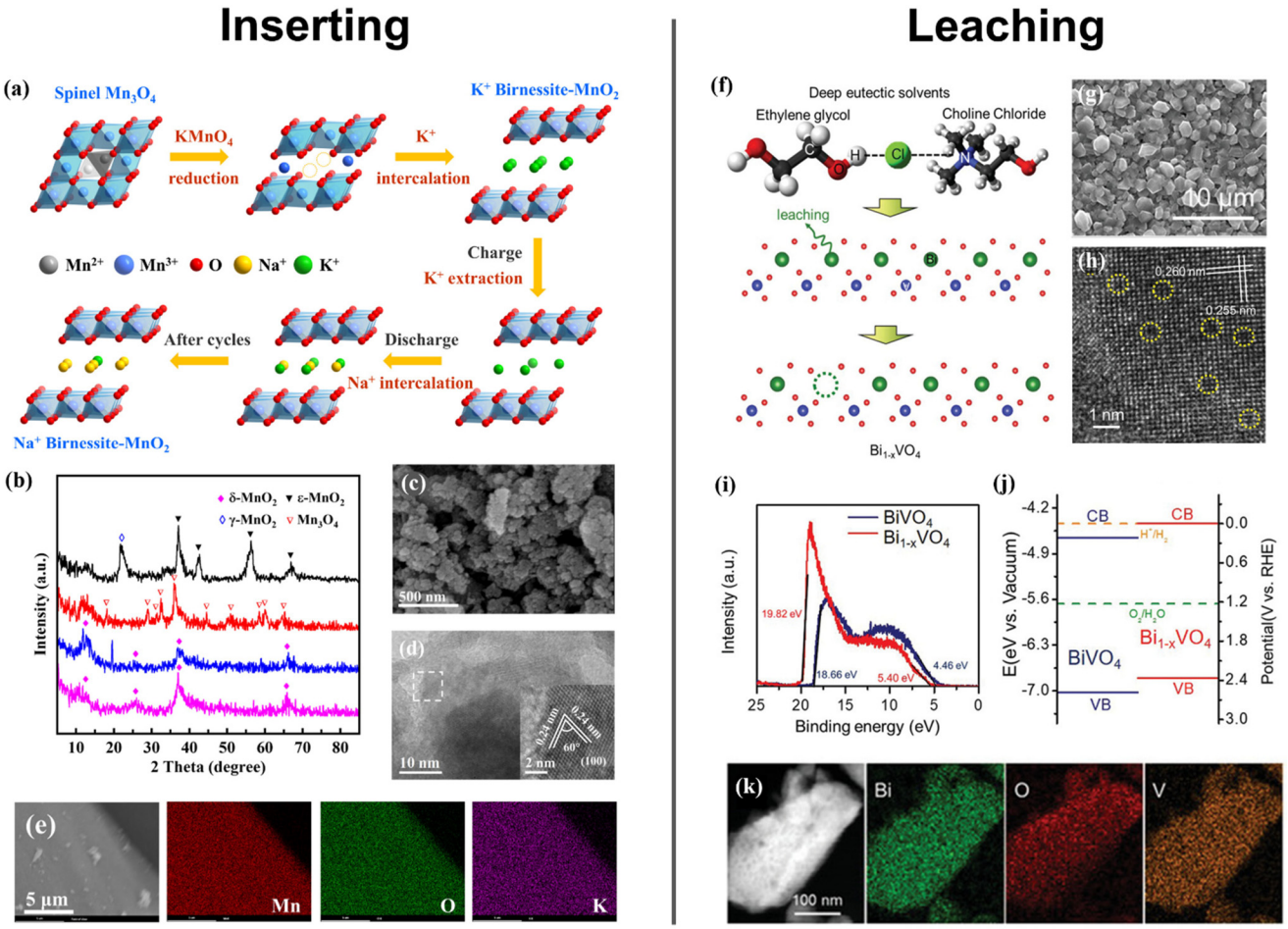

Fig. 5 Inserting and leaching processes conducted in DESs. (a) Schematic illustration for electrochemical reaction process of K inserted birnessite-type MnO_2 electrodes. (b) XRD patterns of MnO_x–CM, MnO_x–CD, MnO_x–CT, and MnO_x. (c) SEM, (d) TEM images and (e) EDX mappings of MnO_x–CM.[109] Reproduced with permission from ref. 109. Copyright 2023 Elsevier. (f) Schematical diagram of Bi leaching from $BiVO_4$ lattices. (g) Top-view SEM and (h) HRTEM images of $Bi_{1-x}VO_4$. (i) Ultraviolet photoelectron spectroscopy (UPS) spectra of $BiVO_4$ and $Bi_{1-x}VO_4$ and corresponding band alignments (j). (k) HAADF–STEM–EDX element mapping of $Bi_{1-x}VO_4$.[31] Reproduced with permission from ref. 31. Copyright 2022, Wiley-VCH.

be performed at higher current densities to achieve fast reaction rates and efficient electrodeposition.[117] In a multi-component system, precise electrodeposition can be realized for preparing complex alloy materials, on account of the inherent high selectivity.

As mentioned above, the intrinsic structure of DESs significantly diverges from that of water, thereby rendering the solvation shell of metal ions within DESs more intricate (depicted in Fig. 7). In an aqueous environment, metal ions are solvated by water molecules, mainly through coordination. Although the interaction in DESs is the same as that in water, there are different ligands (*e.g.*, HBD and HBA), resulting in a dramatic effect on ion mobility. We can simplify electrodeposition into a three-step process:[17]

1. The solvated ion M^+ is adsorbed on the electrode surface. Such a process occurs around the electric double layer.

2. Once the ion M^+ reaches the inner Helmholtz phase, it turns to get electrons from the anode.

3. The ions M^+ are immediately reduced due to the potential across the electrodes.

By comparing the two different processes, we can know the most significant side reactions and avoid the hydrogen evolution reaction during the deposition process. As mentioned above, this advantage is related to the wide electrochemical window of DES, which is caused by its chemical composition. It is worth mentioning that in water–DES systems, the electroplating products are consistent with those in DESs. In other words, the electroplating solution can be diluted by adding water to reduce the viscosity and further increase the reaction rate. This is attributed to the hydrogen bonding network formed by DES with metal ions being stronger than that of water and the latter. However, when the water content reaches a certain level, the solution will lose the properties of a DES and become an ordinary aqueous solution. The limiting water content varies depending on the type of DES, and researchers are also actively exploring it.

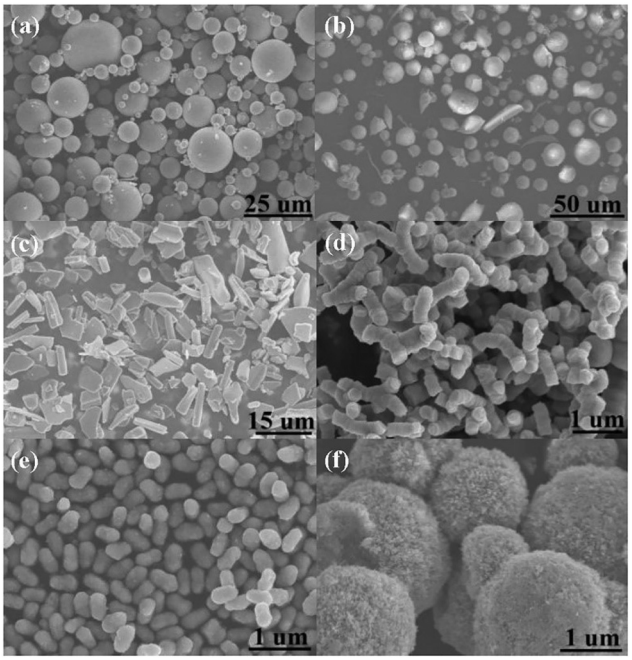

Fig. 6 SEM images for the TiO_2 particles synthesized in different DESs. (a) ChCl/urea, (b) ChCl/glycerinum, (c) ChCl/EG, (d) ChCl/oxalic acid, (e) betaine/oxalic acid, (f) chlorocholine chloride/oxalic acid.[114] Reproduced with permission from ref. 114. Copyright 2018 Elsevier.

4.1. Metals and alloys

Some metals are widely used in everyday materials, so their reduction and purification are of great value. Jovićević *et al.* studied aluminum deposition under constant potential and constant current mechanisms.[118] The shape and size of the deposited aluminum crystal grains depend on the deposition time. The size ranges from nano to micrometers, and from regular crystals to needle-like or sheet-like structures in shape. In addition, the use of the new DES can realize the electrodeposition of aluminum using Al_2O_3 as the raw material.[119] The study by Harb *et al.* showed that by adding fluoride ions to DESs, the structures of Mo complexes were significantly changed.[120] Mo was thus successfully deposited from ethaline onto the nickel substrate at a constant potential. Cyclic voltammetry proved that fluoride changed the electrochemical behaviour of Mo in solution, which is consistent with previous reports. This work paved the way for the possible development of the Mo electrolytic refining process.

In another work, concave-disdyakis triacontahedral (C-DTH) palladium nanocrystals were prepared by shape-controlled electrodeposition in reline.[121] Results showed that the urea adsorbate plays a vital role in the shape evolution, especially in the formation of the specific structure of Pd nanoparticles. The electrical behaviour of Pd is believed to arise through changes in the coordination environment of metal ions. To better explore the growth mechanism of nanocrystals, SEM was used to monitor and characterize the growth process. In the first 10 minutes, the Pd nanoparticles grew to a size of about 45 nm. As the growth time increased, preliminary DTH appeared. Then, it further grew into a truncated C-DTH at 30 minutes and formed a perfect C-DTH shape at 45 minutes. Finally, as time increases, no new structure will appear, but only an increase in size. In addition, there are many elemental

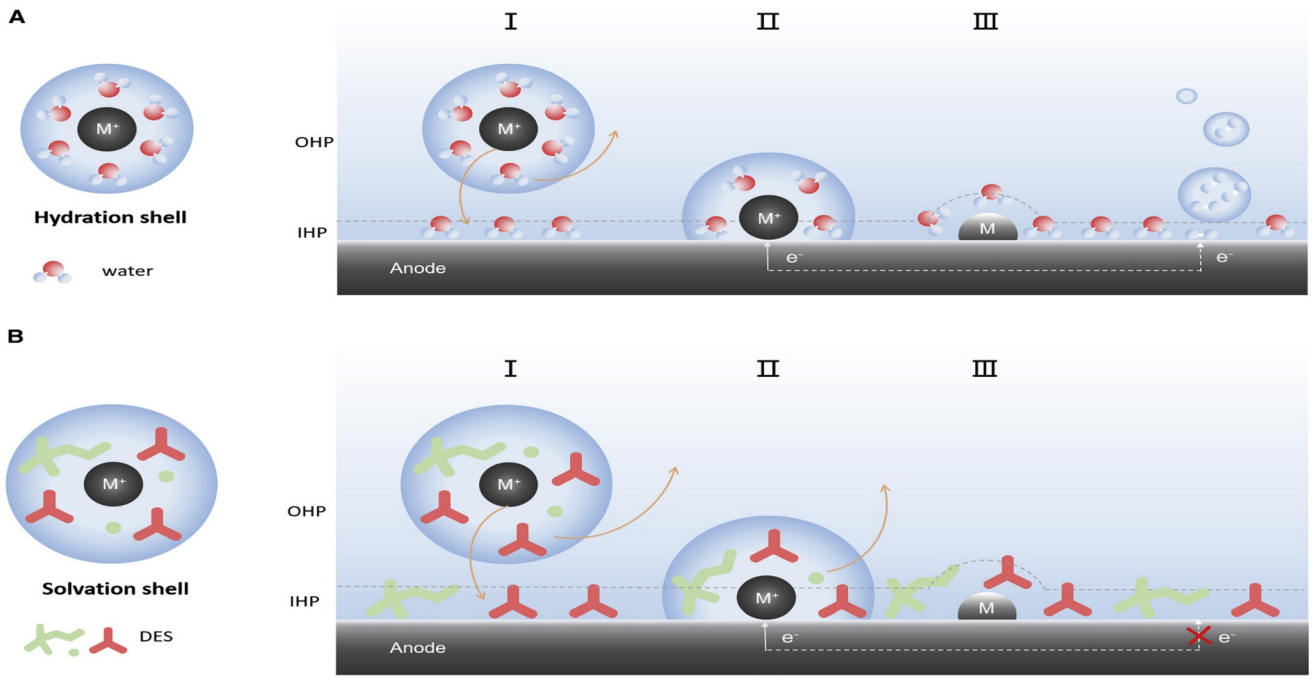

Fig. 7 Interfaces of anode in an aqueous solution (A) and a DES (B). The hydrogen evolution side reaction is hindered by applying DESs in the electrodeposition process.[17] Reproduced with permission from ref. 17. Copyright 2022, Cell press, Elsevier.

metals and alloys that can be electrodeposited in DES, which will be introduced below. All in all, the intervention of DESs can not only realize some specific electrodeposition processes but also accurately control the morphology of synthesized materials.

Ruthenium and its compounds have received increasing attention in recent years because of their high catalytic activity.[122] Magagnin *et al.* reported for the first time the electrodeposition process of ruthenium from ethaline.[123] It was found that sulfamic acid can facilitate the electrodeposition process. The electrochemical experiments carried out proved that the main consequence of the existence of sulfamic acid is the oxidation of Ru(III) to Ru(IV), which indicates the reduction of Ru occurs from Ru(IV) species. The optimized plating conditions can produce a uniform and crack-free Ru coating with a thickness of up to 800 nm.

In addition to transition metals, Sn–Sb alloy powders can be electrodeposited in ethaline.[124] The reduction of Sb(III) and Sn(II) in DES involved an irreversible process controlled by diffusion. When Sb(III) and Sn(II) species coexist, the value of the diffusion coefficient decreases slightly, which may be mainly due to their synergistic effect and the change of metal ion activity coefficient. The electrodeposition potential plays a central role in adjusting the alloy composition but makes little difference to its surface morphology.

Table 1 summarizes metals and alloys deposited in DESs as well as the corresponding operating conditions. As is shown in Table 1, the most favored counter electrode is platinum, while the substrate (working electrode) is variable, depending on the metal deposited. Galvanostatic and potentiostatic modes are desirable for achieving the reducing process. Among the above works, there are several strategies to promote the electrodeposition process, such as increasing temperature and diluting the electrolyte. In some cases there is a single compartment cell, while others involve a binary cell along with a separator. Most of the authors applied the same process when carrying out cyclic voltammetry (CV), linear sweep voltammetry (LSV) and final electrodeposition, and a minority of them used a two-electrode system when electrodepositing.

4.2. Compounds

Compared with alloys, the types and structures of metal compounds are much more complicated. Moreover, the functions of the compounds are more diverse. For example, some materials have excellent electronic band structures and are suitable as photocatalysts. Metal oxides are among the simplest compounds. Wang *et al.* directly prepared nanostructured NiO films through simple and effective electrodeposition.[125] It was proved that the surface morphology and density of the film are related to the operating temperature. The higher the temperature, the lower the viscosity. Therefore, nucleation precedes growth at higher temperatures, so the particle size becomes smaller when deposited at higher temperatures. The light transmittance of the film increases with the increase of the electrodeposition temperature because the purity of the oxide in the product is higher at higher temperatures. Zhang *et al.* introduced a two-step method to prepare metal sulfides. In the first step, Ni nanospheres were deposited on the foamed nickel framework.[126] Subsequently, the resulting metal composite material undergoes a vulcanization reaction at 80 °C. It is worth mentioning that the solvent system used in both steps is a DES (ethaline). The decomposition process of thiourea in ethaline drives time-dependent surface reorganization and phase transitions on Ni substrates, leading to the *in situ* formation of a Ni_3S_2 layer with a controllable structure. The prepared material has a high specific surface area, shows a high specific capacitance of 5.633 mF cm^{-2} at a current density of 10 mA cm^{-2} with good durability, and is expected to be practically applied in high-performance electrochemical devices.

Numerous materials are designed and synthesized to solve energy problems. Some of the work starts with preparing the materials and is then followed by testing their catalytic activity. The design and synthesis of high-efficiency and low-cost bifunctional electrocatalysts for hydrogen evolution reactions and oxygen evolution reactions are essential for electrochemical water splitting related to clean and renewable energy technologies. In the study of Zhang *et al.*, a one-step electrodeposition method of $Fe_xCo_{3-x}(PO_4)_2$ nanosheets filled with 3D microspheres was introduced.[127] The excellent performance can be attributed to the fact that Fe doping changes the active electronic properties of O in the phosphate, thereby achieving the best hydrogen adsorption at the active site. In addition, the unique 3D microsphere structure combined with the internal structure of the 2D nanosheet provides a rich catalytic interface with more active sites and favorable transfer kinetics. The integrated electrode exhibits excellent HER electrocatalytic performance in a wide pH range and has robust catalytic activity for overall water decomposition in alkaline media. In another work, the electrodeposition of P–Co nanoparticles on nickel foam was reported.[128] The prepared catalyst showed excellent performance for both hydrogen evolution reactions and oxygen evolution reactions. It is believed that the above materials will boost the development of hydrogen energy in the future.

There are several conclusions obtained from Table 1:

- Electrode, especially the substrate (cathode), is vitally important and should be considered carefully.
- Thickness and morphology are usually dominated by time, which needs to be controlled based on the target.
- Conditions of CV or LSV experiment and practical deposition processes can be different.
- Galvanostatic and potentiostatic deposition are two different methods, which can be adjusted according to the actual situation during the production process.
- Dilution with water and increasing temperature are two ordinary means to lower the viscosity and accelerate mass transfer.

4.3. Specific structures

Fabricating nanoparticle-modified electrodes is very challenging because it usually involves a multi-step route, such as

Table 1 Metals and alloys deposited in DESs

Metal/alloy	DES			Electrode	Operation	Ref.
	HBA	HBD	Ratio[a]	W/R/C[b]		
Ag	ChCl	EG	1 : 2	Pt|Ag|Pt	The silver was deposited potentiostatically at −35 mV for times ranging from 10 to 6000 s	129
Al	DBU	MTU	1 : 1[c]	Cu|Al|Pt	All processes were performed in an atmospheric environment with a scan rate of 50 mV s^{-1}	119
Au	ChCl	EG	1 : 2	Pt|Ag|Pt	Au coatings were deposited from their respective solutions by immersing the Ni-coated sample in the solution at 80 °C for 45 min	130
Bi	ChCl	EG	1 : 2	Cu|Ag|Pt	Cu atoms were displaced by Bi atoms *via* the consumption of Bi(III) complex ions and the formation of Cu(I) species	131
Cd	ChCl	Thiourea[d]	1 : 2	Steel|Ag/AgCl|Pt	Cd was electrodeposited by employing the DES solution (−0.85 V *vs.* Ag/AgCl, 10 min) on a carbon steel surface	132
Co	ChCl	Urea[d]	1 : 2	Cu|—|Pt	Current densities between 3 and 30 mA cm^{-2} were applied for 30 and 120 min	133
Cr	ChCl	$CrCl_3 \cdot 6H_2O$	2.5 : 1[e]	Steel|—|Pt	The electrodeposition of Cr was performed under a constant 50 mA cm^{-2} and at 40 °C	134
Cu	ChCl	Urea	1 : 2	Au|Cu|Au	Copper electrodeposition process was found to be taking place through the formation of an underpotential deposition adlayer	135
Fe	ChCl	EG	1 : 4	Pt|Ag/AgCl|Fe	The electrodeposition process was operated in the Fe-containing DES under a current density of 50 mA cm^{-2}	136
Ga	ChCl	Urea	1 : 2	Mo|Ag|Pt	Electrodeposition of the Ga films was performed under −1.1 V (60 °C) at a rotation speed of 300 rpm for 30 min	137
In	ChCl	Urea	1 : 2	Mo|—|Pt	Bulk electrodeposition of indium was carried out at 80 °C in the In-containing DES at 10, 30, and 50 mA cm^{-2} for 60 min	138
Mn	ChCl	EG	1 : 2	Cu|Ag/AgCl|C	Electrodeposition was carried out at 50 °C under a constant potential of −1.50 V	139
Ni	ChCl	EG	1 : 2	Al|Ag|Pt	Galvanic deposition process of Ni was carried out in Ni-containing DES at 50 °C for 4 h	140
Pb	ChCl	Urea	1 : 2	Cu|Ag|Pb	Electrodeposition process was conducted *via* potentiostatic or galvanostatic electrolysis in the baths steadily stirred under 90 °C	141
Pd	ChCl	Urea	1 : 2	Au|Ag|Pt	The electrodeposition of Pd on Au was operated around −0.2 V and an underpotential deposition around 0 V at 60 °C	142
Pt	ChCl	Urea	1 : 2	GC|Pt|Pt	Potential scan range of −1.5 to −0.2 V (80 °C), scan rate of 50 mV s^{-1} and CV number of 80 cycles	143
Re	ChCl	Urea	1 : 2	Cu|Ag|Pt	Electrodeposition was carried out under galvanostatic (0.3 and 0.5 A d^{-1} m^{-2}) and potentiostatic (−1.2 and −1.6 V) modes under stirring for 30 min	144
Ru	ChCl	EG	1 : 2	Cu|Pt|C	Both galvanostatic and potentiostatic deposition from Ru-containing DES was performed under 80 °C	123
Sb	ChCl	EG	1 : 2	Ti|Ag|Pt	The electrodeposition process was carried out from 10 to 50 mA cm^{-2} for 5 h at different temperature	145
Sm	ChCl	Urea	1 : 2	C|Ag/AgCl|Pt	Metal and alloy deposits were obtained during a voltammetric hold potential at −1.9 V under stirred conditions for 30 min	146
Sm–Co						
Sn	ChCl	EG	1 : 2	Ni|-|Sn	At different temperature (40–80 °C), the constant current was supplied by a DC power at 20 mA cm^{-2} for 1 h	147
Zn	ChCl	Urea[d]	1 : 2	Steel|Ag|Pt	The deposition occurred in Zn-containing DESs at 50 °C, on mild steel at I = 3 mA cm^{-2}	148
As–In	ChCl	EG	1 : 2	Cu|Ag|Pt	Constant potentials (−0.5 to −1.03 V) were applied at 80 °C with the deposition charge density of 2 C cm^{-2}	149
Au–Mn	ChCl	Urea	1 : 2	Au|Au|Pt	Au–Mn was electrodeposited potentiostatically (−0.7 to −1.9 V) for 1 hour	150
Cd–Zn	ChCl	EG	1 : 2	Cu|Ag/Ag^+|Pt	The electrodepositions were conducted at the constant potentials in the range from −1.3 to −1.7 V for 6 C cm^{-2} at 50 to 90 °C	151
Ce–Ni	ChCl	EG	1 : 2	Steel|Pt|Pt	Electrodeposition process was carried out using the chronopotentiometry method (10 mA cm^{-2}) up to a charge of 100 mA h	152
Co–Cr	ChCl	EG	1 : 2	Brass|—|C	Electrodeposition of Co–Cr alloys was obtained by using direct current and pulsed electrodeposition techniques	153
Co–La	NaBr	Urea	—	Steel|Hg/HgO|Pt	La–Mo alloy was deposited from different current density 10 to 40 mA cm^{-2} at 130 °C	154
	$CoSO_4$ $LaCl_3$					
Co–Nd	ChCl	Urea	1 : 2	Cu|Ag|W	Co–Nd alloy was obtained by electrodepositing under constant current density (50 to 125 mA cm^{-2} at 100 °C)	155
Cu–Mn	ChCl	EG	1 : 2	Cu|—|Pt	Pulse current electrodeposition (30 min) was conducted in which each cycle consisted of 1 s of low current, followed by 1 s of high current	156
Cu–Ni	ChCl	Urea	1 : 2	Ni|Ag|Pt	Cu–Ni alloy was electrodeposited from −0.9 V to −1.2 V in the leached electrolyte at 70 °C for 1 h	157
Cu–Zn	ChCl	Urea	1 : 2	Fe|Ag|Pt	Electrodeposition was conducted at the range of potentials −0.80 to −1.15 V, and 70 °C for 2 h	158

Table 1 *(Contd.)*

Metal/alloy	DES HBA	DES HBD	DES Ratio[a]	Electrode W/R/C[b]	Operation	Ref.
Fe–Co	ChCl	EG	1 : 2.24	Cu|—|Fe	The alloy was electroplated using a direct current 67 mA cm^{-2} for 2 to 20 min (at 100 °C)	159
Fe–Cr	ChCl	EG	1 : 3	Brass|—|Cr	Fe–Cr alloy was prepared by electrodeposition in DES by varying cell voltage (2.4 to 2.8 V) and temperature (60 to 80 °C)	160
La–Ni	Acetamide	Urea	—	Cu|—|C	The alloys were obtained by potentiostatic electrolysis under an Ar atmosphere for 25 min (at 80 °C)	161
Sm–Fe Gd–Co	NaBr KBr					
Ni–P	ChCl	EG	1 : 2	Brass|Ag|Ni	Ni–P alloys were obtained at a potential of −0.7 V for 10 min (30 ± 2 °C)	162
Ni–Ta	ChCl	Urea	1 : 2	Cu|Ag|Ti	Electrodeposition was performed at potentiostatic (−0.3 V) and galvanostatic (1 mA cm^{-2}) conditions for a duration of 30 minutes with stirring at 400 rpm	163
Pd–Ag	ChCl	Urea	1 : 2	Cu|Pt|Pd	Alloys were obtained by pulse plating and potentiostatic deposition for 15 or 30 min	164
Pd–Pt–Ag						
Sn–Bi	ChCl	EG	1 : 2	Au|Ag|Pt	Different coatings were deposited potentiostatically on substrates at different potentials (−0.4 to −0.6 V)	165
Sn–In	ChCl	EG	1 : 2	Cu|—|Pt	Galvanostatic (1 and 25 mA cm^{-2}) deposition was performed for 20 min at 25 to 60 °C	166
Zn–Mn	ChCl	Urea	1 : 2	Steel|Hg/Hg_2Cl_2|Zn	Zn–Mn alloy was deposited by a charge density of 20 C cm^{-2}, at 70 °C	167
Zn–Ti	$ZnCl_2$	Urea	1 : 3	Cu|Pt|C	Zn–Ti alloy was prepared at deposition potential of −1.3 to −1.8 V for 2 h (80 °C)	168
Pr–Mg–Co	ChCl	Urea	1 : 2	Cu|Ag|Pt	The optimum coating was obtained at −1.05 V for 20 min	169
Zn–Ni–P	ChCl	Urea	1 : 2	Cu|Ag|Ni	Ni–Sn–P alloys were obtained by using constant potentials (−0.6 to −0.8 V) with total charge density of 4 C cm^{-2} at 60 °C	170

[a] Molar ratio of HBA : HBD. [b] W|R|C refers to working, reference, and counter electrode, respectively. [c] More than one HBD. [d] Means more than one ratio. [e] Electrolyte contains additional water; DBU: 1,5-diazabicyclo[5.4.0]-5-undecene, MTU: methylthiourea, GC: glassy carbon.

chemical synthesis, purification, and final embedding on the electrode surface. Moreover, it always requires high temperatures. By using DESs as electrolytes, electrodeposition can be operated at room temperature, achieving an all-in-one process. Renjith and Lakshminarayanan reported a single-step electrochemical preparation and the *in situ* deposition of thin clusters of cobalt nanoparticles on the electrode surface in maline.[171] The thickness of the nanoparticle clusters ranges from 20 to 90 nm. Although the catalyst loading is very low, the cobalt nanoparticles on the dense graphite flakes can obtain an oxygen evolution reaction (OER) current of 10 mA cm^{-2} at a very low overpotential of 350 mV, which indicates that it is a good potential anode material for the oxygen evolution reaction.

As mentioned above, the two precursors in DES are not necessarily reduced in the form of alloys. Mohan *et al.* synthesized multilayer Ag–Co corn-shaped material by a pulse technique.[172] The synthesized materials exhibited a maximum giant magnetoresistance value of 9.94% at room temperature. In some cases, DES can achieve material composites that are difficult to complete in water systems. It has proved difficult to co-deposit SiO_2 particles into a metal matrix in an aqueous solution. Liang and coworkers demonstrated the pulse electrical co-deposition of nano-sized SiO_2 particles and a Ni matrix in ethaline.[173] SiO_2 nanoparticles exhibit excellent dispersion stability in DES, which is very important. In addition, the presence of SiO_2 nanoparticles has a significant impact on the nucleation mechanism of Ni. Increasing the content of SiO_2 in the composite material can significantly improve the corrosion resistance of the coating.

A simple one-step electrochemical deposition strategy of self-supporting Co–O and Co–Se hybrid films in reline has been reported.[174] DES was believed to play an important role in forming porous nanostructures, and these pores significantly promote the intrinsic catalytic activity of the material. The Co–Se component in the hybrid film was inherently unstable under OER conditions and transformed into Co–O species with enhanced surface oxygen vacancies. Therefore, the prepared material shows high catalytic performance and robust durability for both HER and OER.

The core–shell structure is a more complex structure than ordinary composites. It contains an inner core and a uniform outer thin layer. The synthesis of this special structure material can be achieved by electrodeposition. Pd@$Pd(OH)_2$ nanoparticles were electroplated onto the glassy carbon electrode in reline.[175] The core–shell structure is so distinct that it shows clearly in scanning electron microscopy. Interestingly, the small amount of water (0.15% by Karl Fischer coulometric titration) inherent in DES plays a significant role in forming the outer shell. The corresponding chemical reaction formula is as follows.

$$Pd^{2+} + e^- \rightarrow Pd \quad (4)$$

$$2H_2O + 2e^- \rightarrow H_2 + 2OH \quad (5)$$

$$Pd^{2+} + 2OH^- \rightarrow Pd(OH)_2 \quad (6)$$

Au@Pd can also be synthesized by a similar electrochemical method.[176] The hydrogen bond donor (ethylene glycol) used in the work of Lakshminarayanan and Renjith is different from that of the above work (urea). Ethylene glycol itself has a good reducing ability so that no additional water is required. Therefore, the outer shell layer is elemental Pd instead of $Pd(OH)_2$.

4.4. Coating and etching

Etching and coating are two reversed processes, which can both be achieved by using appropriate DES (Fig. 8). In Xu's work, an *in situ* DES etching strategy was developed to prepare NiP encapsulated in P,O co-doped carbon nanosheets.[177] DES

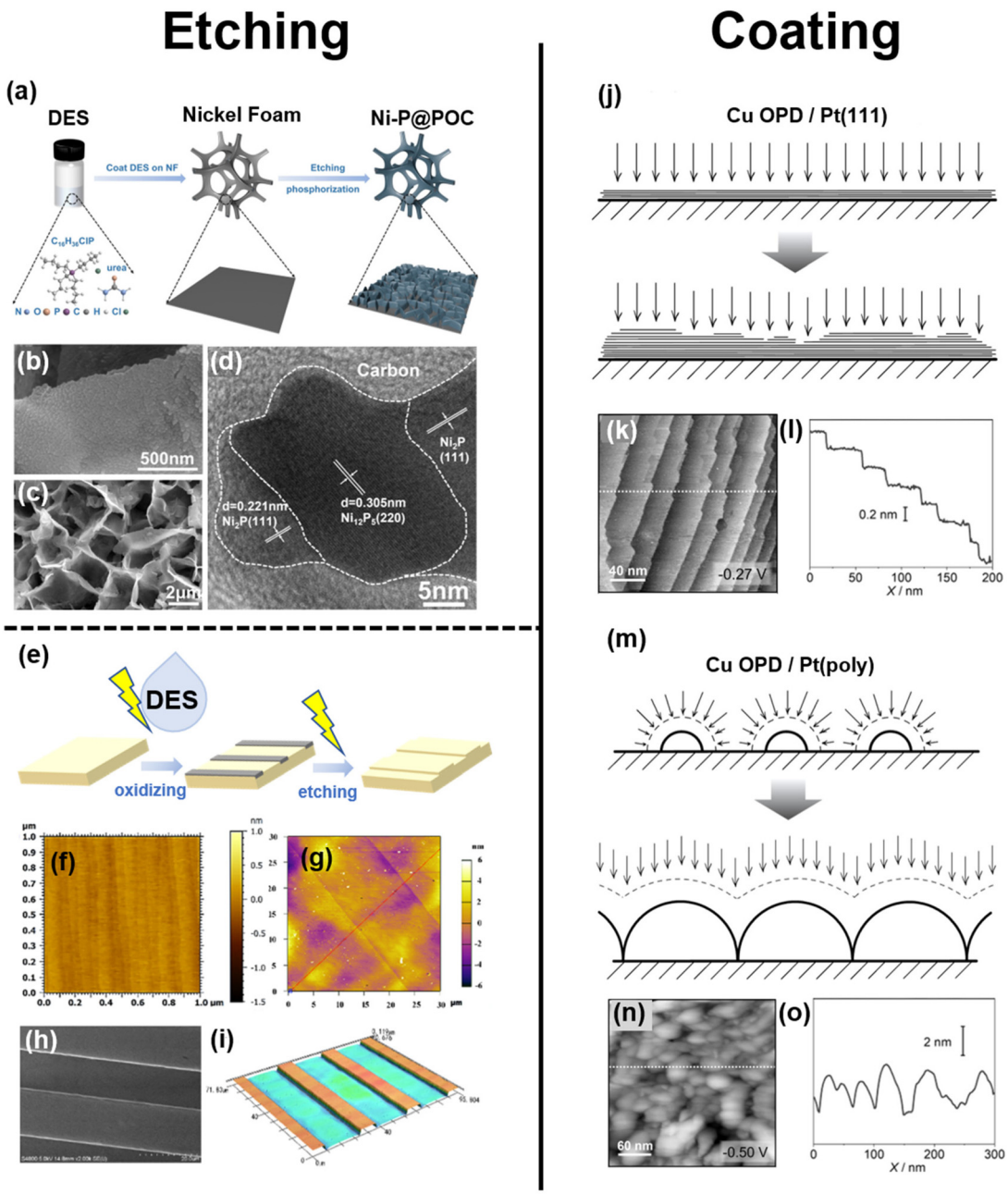

Fig. 8 Etching and coating processes conducted in DESs. (a) Schematic of t-Ni–P@POC synthesis process. (b) and (c) SEM images of t-Ni–P@POC at different magnifications. (d) TEM image of t-Ni–P@POC.[177] Reproduced with permission from ref. 177. Copyright 2022, Wiley-VCH. (e) The DES-assisted etching process. (f) and (g) AFM images of bare and oxidized GaN substrates. (h) SEM image of patterned GaN after etching. (i) Laser scanning microscopy image of grooves prepared at −0.2 V.[178] Reproduced with permission from ref. 178. Copyright 2020, IOP publishing. (j) Schematic representation of planar diffusion mechanism in the case of Pt(1 1 1). (k) *In situ* STM-image of layered Cu on Pt(1 1 1) at −0.27 V. (l) The cross-section profile was obtained along white dashed line in (k). (m) Mechanism of forming hemispherical plane on a Pt(poly). (n) *In situ* STM-image of semispherical Cu on Pt(poly). (o) The cross-section profile was obtained along white dashed line in (n).[179] Reproduced with permission from ref. 179. Copyright 2022 Elsevier.

composed of tetrabutylphosphonium chloride and urea (molar ratio 1 : 1) serves not only an etchant to extract Ni^{2+} from nickel foam, but also a phosphorus source to form nickel phosphide uniformly embedded in the carbon film *in situ* to produce a sheet-like structure. Another example showcases the typical process in the semiconductor industry, realizing nanoscale surface roughness with desirable flatness.[178] Hu and coworkers proposed a smooth etch strategy by in-depth study of the interfacial reactions of GaN photoanodes in DES and other aqueous electrolytes. With the increase of the anodic potential, hydroxyl anions and H_2O molecules first react with holes (h^+) on the GaN interface, initiating GaN oxidation by generating hydroxyl radicals ($OH^•$). It was found that etching is the result of the synergy of interfacial reactions, including GaN oxidation, oxide film formation and dissolution, and side reactions. This method allows the preparation of groove structures most typical of GaN-based devices with nanometer-scale surface flatness, such as insulated-gate bipolar transistors.

In contrast to the etching process, Zaytsev *et al.* studied the electrodeposition of Cu in DES, on single crystal Pt(1 1 1) and polycrystalline Pt(poly) planes.[179] The underpotential deposition process of Cu on Pt(1 1 1) surface in DES was observed for the first time, in which the surface morphology and (co) adsorption of solution components played important roles. Furthermore, the mechanism of Cu electrodeposition in DES was found to be determined by the surface structure: STM data demonstrated the layer-by-layer growth of 2D Cu deposits on Pt(1 1 1), while the resulting Cu deposits on Pt(poly) had characteristics of grain-like morphology.

We usually use platinum as a counter electrode because of its stable chemical properties, but is this the case? A novel work showed that the dissolution behaviour of the electrode in

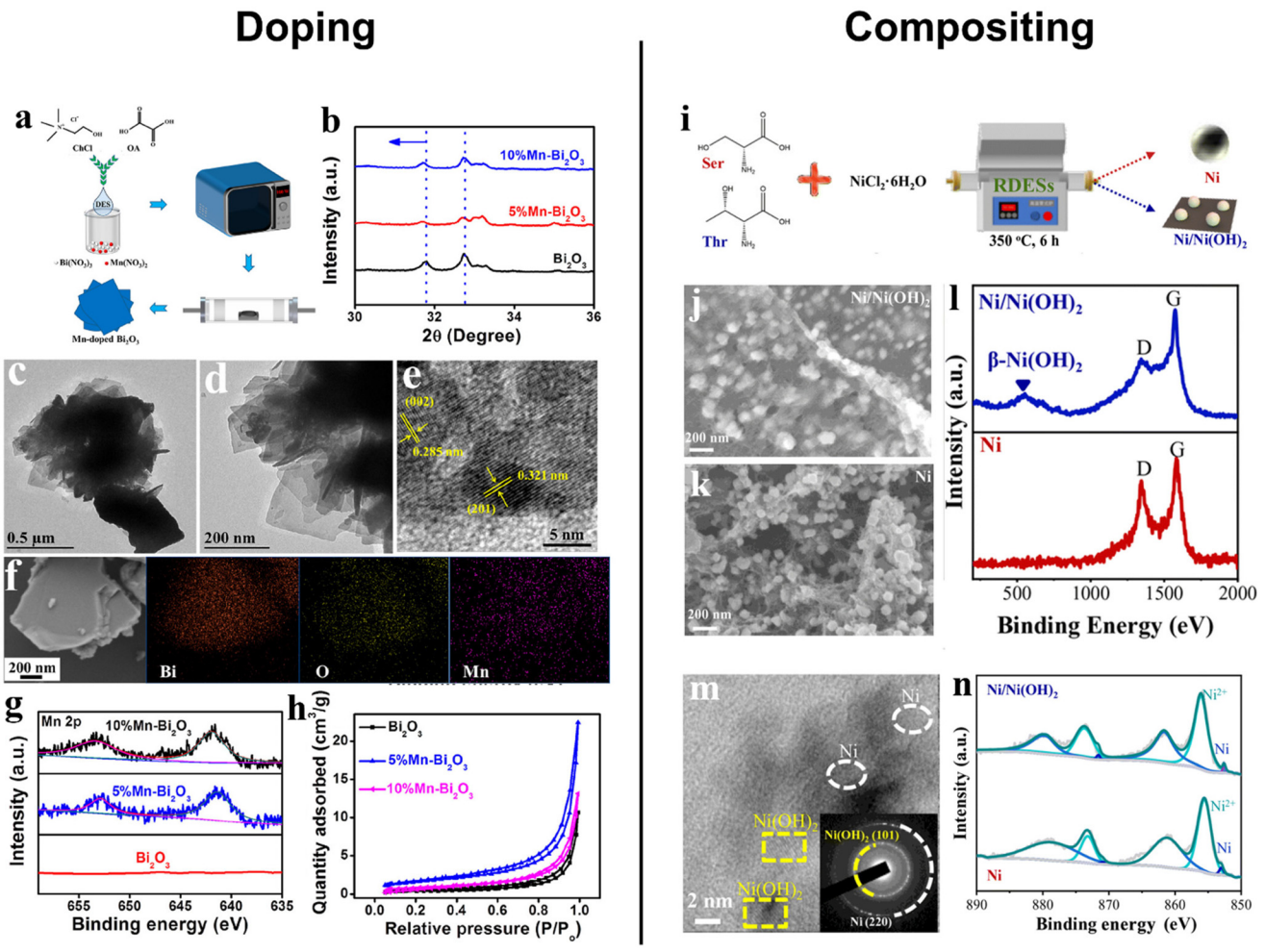

Fig. 9 Doping and compositing conducted in DES. (a) Schematic illustration of the Mn-doped Bi_2O_3 nanosheets synthesis. (b) XRD patterns of 10% Mn–Bi_2O_3, 5% Mn–Bi_2O_3 and Bi_2O_3. (c), (d) TEM images, (e) HRTEM, and (f) SEM and corresponding EDX mappings of 5% Mn–Bi_2O_3. (g) XPS spectra of 10% Mn–Bi_2O_3, 5% Mn–Bi_2O_3 and Bi_2O_3 (Mn 2p). (h) N_2 adsorption–desorption isotherms of Bi_2O_3, 5% Mn–Bi_2O_3 and 10% Mn–Bi_2O_3.[194] Reproduced with permission from ref. 194. Copyright 2022, American Chemical Society. (i) Schematic diagram of the formation of Ni nanoparticles and a 2D $Ni/Ni(OH)_2$ heterostructure in amino acid-based DESs, respectively. SEM images of (j) Ni nanoparticles and (k) $Ni/Ni(OH)_2$ nanosheets. (l) Raman spectra of $Ni/Ni(OH)_2$ and Ni. (m) HRTEM image of $Ni/Ni(OH)_2$ nanosheets, inserted: the related small-angle X-ray diffraction image. (n) XPS spectra of the Ni and $Ni/Ni(OH)_2$ samples (Ni 2p).[195] Reproduced with permission from ref. 195. Copyright 2022, Royal Society of Chemistry.

the composite electrodeposition process still needs further study. Lu *et al.* reported the dissolution mechanism of a platinum electrode and silver reference electrode during nickel–carbon composite electrodeposition in DESs.[180] When the pre-prepared nickel–carbon particles were added to ethaline with Pt as the counter electrode and Ag as the reference electrode, a platinum-based composite material with a "cauliflower" morphology could be deposited. The excellent catalytic performance is attributed to the dissolution–electrodeposition of the Pt and Ag electrodes during the composite electrodeposition process. Density functional theory calculations further show that Pt/Ag interact with chlorine atoms on their surface, and the added activated carbon particles have a significant effect on the dissolution process. Lu's work provides a new method for preparing Pt-based composite materials, and also indicates that the dissolution behaviour of the Pt counter electrode and the Ag reference electrode should be taken into consideration when designing the electrodeposition reaction.

DFT calculation is a very effective way to study the properties of a DES, such as showing the internal structure, predicting viscosity, *etc*. Zhang *et al.* investigated the molecular structure of DES (ChCl and $MgCl_2{\cdot}6H_2O$).[181] The result shows that the main chemical species of the above system is $[MgCl_m(H_2O)_{6-m}]^{2-m}$ and $[Ch_xCl_y]^{x+y}$ clusters. Additionally, the active magnesium complexes in the electrochemical process were determined, and the electrochemical process mechanism between choline chloride and magnesium chloride hexahydrate was explained.

5. Calcination

The composition of DESs is remarkably diverse, encompassing more than 40 metallic elements, and there is even a report on a uranium-based DES.[182] On the other hand, DESs provide a homogeneous and stable liquid environment in regard of precursors. Furthermore, the heterogeneity of DESs makes them suit-

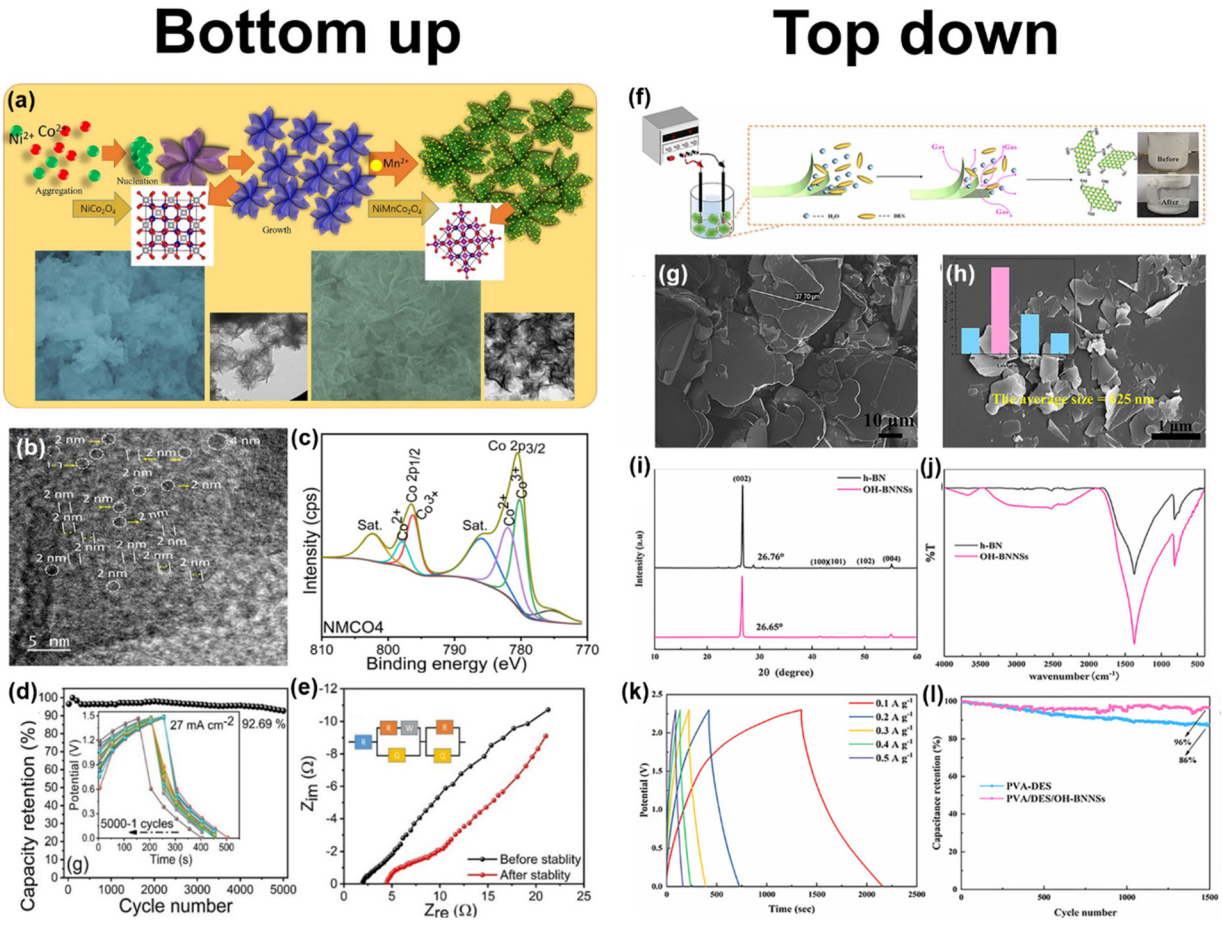

Fig. 10 Comparison of bottom-up and top-down methods for synthesizing materials in DESs. (a) Schematic diagram of the formation of $Ni_{1-x}Mn_xCo_2O_4$ composite nanoflakes. HR-TEM image (b) and high-resolution XPS spectra (c) of the $Ni_{0.8}Mn_{0.2}Co_2O_4$ composite, Co 2p. (d) Specific capacitance with respect to various current densities of solid-state hybrid $Ni_{0.8}Mn_{0.2}Co_2O_4$//AC (activated carbon). (e) Nyquist plots of hybrid supercapacitor after and before cycling stability of the hybrid $Ni_{0.8}Mn_{0.2}Co_2O_4$//AC device.[196] Reproduced with permission from ref. 196. Copyright 2022, Wiley-VCH. (f) Schematic representation of the mechanism of electrochemical exfoliation in DES. SEM images of bulk h-BN (g) and hydroxylated boron nitride nanosheets (h), inset: the histogram of statistical size. XRD patterns (i) and FT-IR spectra (j) for bulk h-BN and PVA/DES/OH-BNNSs. (k) Galvanostatic charge–discharge behaviors of supercapacitors with PVA/DES/OH-BNNSs. (l) Cycling stability of supercapacitors with PVA/DES/OH-BNNSs and PVA/DES gel polymer electrolytes.[197] Reproduced with permission from ref. 197. Copyright 2022, American Chemical Society.

able for tuning the morphology of the product at the nanoscale. Based on the thermal stability studies mentioned above, the calcination method is often adopted to prepare the target materials.

5.1. Carbon materials

In some cases, the DES itself serves as the carbon source, and no other precursor is needed. Cai *et al.* reported a direct calcination method to prepare N-doped porous carbon.[183] The DES used in this work was composed of glucose and urea, which is low cost and green. Miniature supercapacitors based on N-doped carbon nanosheets exhibit a specific capacitance of 23.2 mF cm^{-2} at 0.2 mA cm^{-2}. In addition, such calcination methods can be applied to prepare mesoporous silica.[184] Compared with those based on surfactant or ionic liquid, DES-templated synthesis is cheaper and more environmentally friendly. Porous carbon turns to form a coating layer, which is beneficial for the fabrication of multilayer structures and core–shell structure materials.[185,186] Wen *et al.* synthesized $NaTi_2(PO_4)_3$/C by calcinating choline chloride/triethanolamine DES.[187] The 3D layered porous material that has abundant macropores was an anode material for sodium-ion batteries.

Graphitic carbon nitride (g-C_3N_4) as a kind of metal-free n-type semiconductor has been considered a promising light photocatalyst. However, the photocatalytic performance of g-C_3N_4 is far from satisfactory, because the random transfer of charge carriers in the plane leads to a low conversion rate. Therefore, some oxides, such as ZrO_2 and CuO, can be used as cocatalysts to improve the photocatalytic performance of the composites.[188,189] During calcination, the urea in the DES decomposes to produce g-C_3N_4 accompanied by the generation of ZrO_2, making the composites extremely stable. The prepared material shows high activity for OER and NRR reactions. However, in the case of CuO, the metal oxide and C_3N_4 were not generated from the DES at the same time. The DES was used to dope Cl^- into the CuO lattice structure, and then the Cl^--doped CuO was combined with the pre-prepared C_3N_4 *via* an ultrasonication and mixing method. In addition to g-C_3N_4, borides can also be prepared from DESs by calcination.

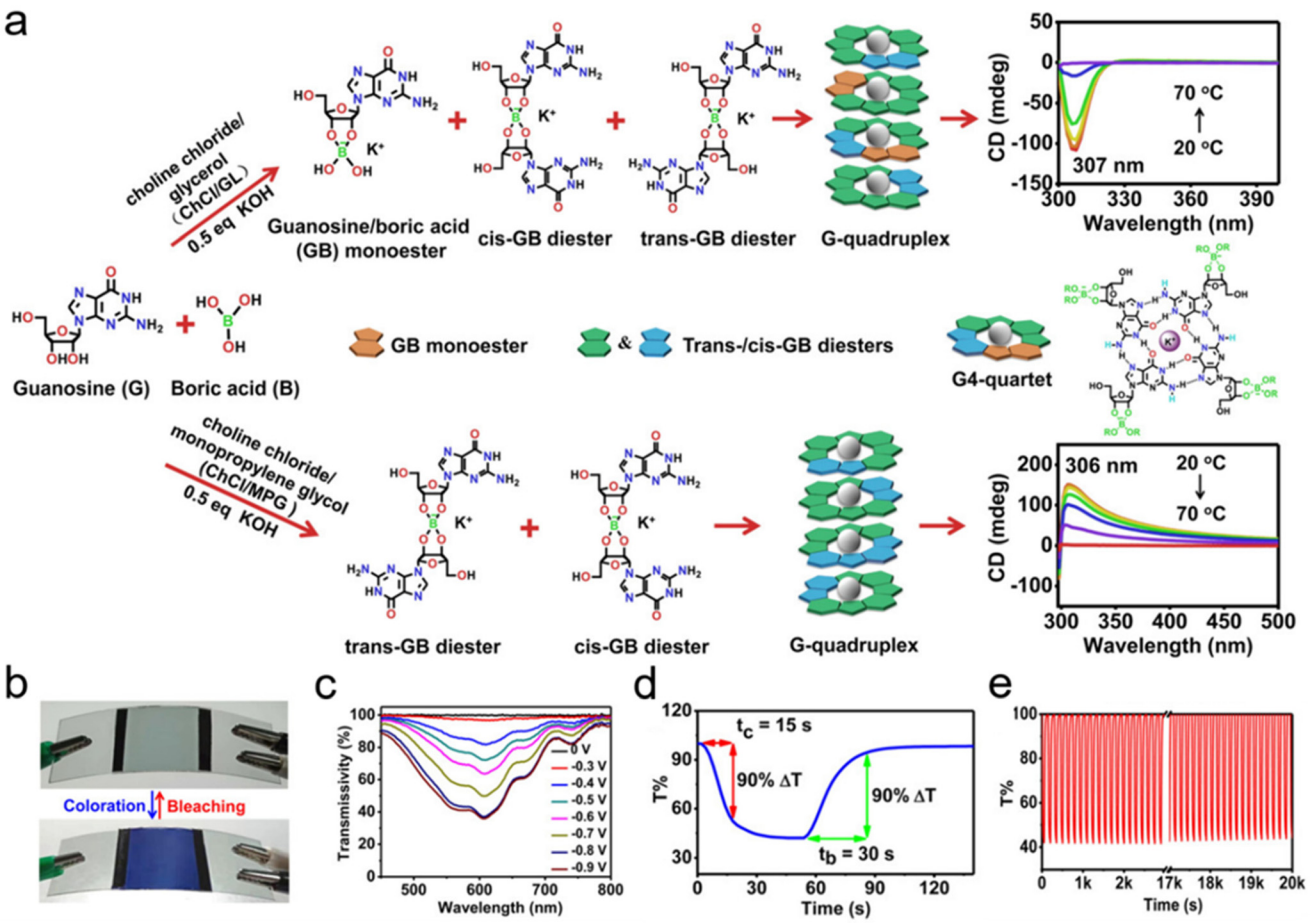

Fig. 11 (a) The scheme of a possible mechanism for gelation process *via* formation of guanosine/boric acid (GB) borate esters and subsequently G4-quartets. Inset: the CD spectra. (b) Photographs of the ChCl/MPG ECD at −0.7 V for colouring and 0 V for bleaching. (b) UV-vis spectra at various voltages for the ECD based on the hybrid GB/MPG eutectogel. (c) Transmittance responses of the ChCl/MPG ECD at −0.7 V for colouring and 0 V for bleaching. (d) *In situ* transmittance response of the ChCl/MPG ECD over 100 coloring-bleaching cycles.[198] Reproduced with permission from ref. 198. Copyright 2020, Wiley-VC. (e) *In situ* transmittance response of the ChCl/MPG ECD over 100 cycles, coloring for 60 seconds with a potential at 0.7 V, and bleaching for 150 seconds with 0 V applied.

5.2. Metal-based materials

In addition to amorphous carbon materials and their composite materials, compounds with crystal structures can be prepared by calcination in DESs as well.[190,191] Furthermore, designing the reacting conditions makes it possible to control the morphology of the synthesized products. George *et al.* reported metal oxide particles as precursors to prepare target materials, which is unusual in the synthesis based on DESs.[192] They smartly used the decomposition of the carboxylic acid component in the DES to synthesize co-oxides. The electrode modified by nano-$MgFe_2O_4$ showed a high sensitivity for detecting nitrofurantoin and 4-nitrophenol.

In order to enhance the photocatalytic efficiency of g-C_3N_4, Mou *et al.* synthesized g-C_3N_4/ZrO_2 layered materials with the assistance of DES ($ZrOCl_2 \cdot 8H_2O$/urea).[189] Studies have shown that when the ZrO_2 content in the composite material is 30 wt%, the optimal NH_4^+ yield can reach 1446 μmol L^{-1} h^{-1}. The apparent quantum efficiency at 400 nm exceeds 2.14%, which is 7.9 times higher than the original g-C_3N_4, and 27.5 times that of ZrO_2. In addition, the introduction of amorphous ZrO_2 inhibits the generation of hydrogen and can promote rapid photogenerated electron transfer.

The materials synthesized by calcining DESs can also be used in traditional catalytic reactions. The selective oxidation of alcohols to the corresponding aldehydes and ketones is of great significance in academic and industrial fields. Tao *et al.* prepared an excellent nanostructured catalyst of cobalt nanoparticles supported on nitrogen-doped carbon (Co–N–C).[193] The results show that the optimized Co–N–C exhibits excellent catalytic performance in the selective oxidation of aryl alcohols and alkyl alcohols, enabling the corresponding aldehydes and ketones to reach >99% yield. Such high catalytic activity is believed to be due to the synergistic interaction between the nitrogen-doped carbon support and the Co–N species. Interestingly, the magnetically recyclable Co–N–C catalyst can be easily separated from the reaction system by using an external magnetic field.

Doping and compounding are common means of modifying materials, and this section starts by presenting two related studies in the context of calcination (Fig. 9). Ying *et al.* designed Mn-doped Bi_2O_3 nanosheets, which were fabricated by using a DES for the first time.[194] The results showed that the introduction of Mn into Bi_2O_3 can significantly enhance the faradaic efficiency of the nitrogen reduction reaction by suppressing the unfavorable hydrogen generation. Wei *et al.* investigated the effects of chain length, functional group substitution, and molar ratio on the thermodynamic stability of DESs based on different amino acids.[195] Ni and composite Ni@$Ni(OH)_2$ samples were prepared by a one-step annealing process, which exhibited quite good oxygen evolution reaction performance in alkaline solutions.

5.3. Bottom-up and top-down

In the above content, we mainly introduced solvothermal, electrochemical and calcination methods for synthesizing materials. To finalize this section, two opposite processes are compared, illustrating strategies for designing task-specific DESs to prepare target materials (Fig. 10). In Shinde's study, nanoparticle-decorated ultrathin $Ni_{1-x}Mn_xCo_2O_4$ nanosheets (NPs@NFs) were bottom-up synthesized by adjusting the molar ratio between Mn and Ni in the DES.[196] The unique and highly porous NPs@NFs nanostructure helps to increase the overall surface area of the material, while Mn, Ni, and Co ions constitute its redox activity ability, thereby enhancing the electrochemical activity of the material. This Ni–Mn–Co_2O_4 hybrid nanostructure exhibits excellent performance with a high specific capacity of 761 mA h g^{-1} at a relatively high current density of 30 mA cm^{-2} and a cycle-retained rate of 92.86%. Furthermore, the hybrid asymmetric supercapacitor ($Ni_{0.8}Mn_{0.2}Co_2O_4$//AC) device exhibits an extended potential window of 1.5 V, yielding an ultrahigh energy density of 66.2 W kg^{-1}. Top-down preparation of few-layer hydroxylated boron nitride nanosheets (OH-BNNS) from bulk material is highly valued and promising, although an efficient method still remains challenging. Shan and co-workers developed a one-step preparation process of OH-BNNS assisted by an aqueous DES electrolyte-assisted exfoliation and oxidation process.[197] The results showed that the obtained OH-BNNS had an average lateral dimension of 625 nm and a thickness of six layers. Adding OH-BNNSs and DES into polyvinyl alcohol (PVA) substrates creates composite gel polymer electrolytes for solid-state flexible supercapacitors. Moreover, a symmetric solid-

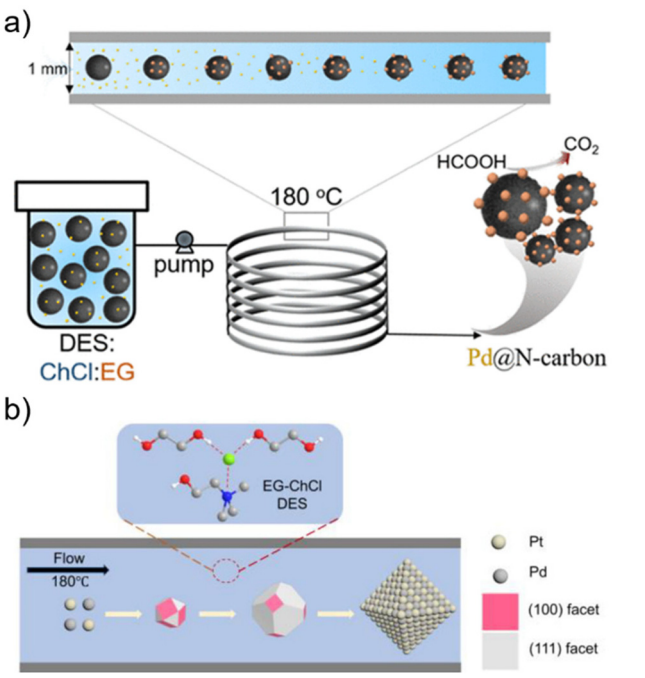

Fig. 12 One-step flow and shape-controlled synthesis of nano particles in DES. (a) Schematic illustration of combining DES solvothermal and microfluidic technology to continuously produce nano-sized Pd@N-carbon.[209] Reproduced with permission from ref. 209. Copyright 2020, American Chemical Society. (b) Shape-controlled PtPd nanocrystal synthesis in flowing ethaline.[25] Reproduced with permission from ref. 25. Copyright 2023, American Chemical Society.

state flexible supercapacitor composed of activated carbon electrodes and PVA/DES/OH-BNNSs gel polymer electrolyte emerged with a wide voltage window of 2.3 V and a high specific capacitance of 151.22 F g at 0.1 A g for 1500 cycles with a 98% maintenance of capacity.

6. Supramolecules and polymers in DES

With the development of eutectic systems, concepts such as eutectogel and supramolecular DES were proposed.[7,8] DES-based gel, further referred to as eutectogels, serves as a promising candidate for solid composite electrolytes. These robust composite electrolytes demonstrate satisfactory thermal stability up to more than 100 °C, along with an extensive electrochemical stability range and elevated ionic conductivity at ambient temperatures. In a work, Liu *et al.* reported a complex of natural guanosine and H_3BO_3, which showed excellent gelling ability in DESs.[198] In this case, the reactants guanosine, H_3BO_3, and KOH in DES ChCl/MPG turn to produce an anionic guanosine boronic acid diester complex (GB), which is further templated by K^+ to form a hydrogen bond G-quartet structure (G4). The G4-quadruplex spontaneously stacks into a column G-quadruplex structure generated by physically entangled fibres that constitute the ChCl/MPG eutectogel (Fig. 11a). Conversely, mixing guanosine, H_3BO_3, and KOH in a glycerol-based DES resulted in GB monoester and GB diester complexes. This further leads to a more complex G-quadruplex structure with a different supramolecular chirality (Fig. 11a).

Sometimes, eutectogels combined with other sustainable materials (such as biomass) exhibit enhanced mechanical properties. A polymerized high-performance sensor incorporating polymerized DES into delignified wood has attracted public attention.[199] The retained orientation and the strong hydrogen bonding interactions between the cellulose-rich template and

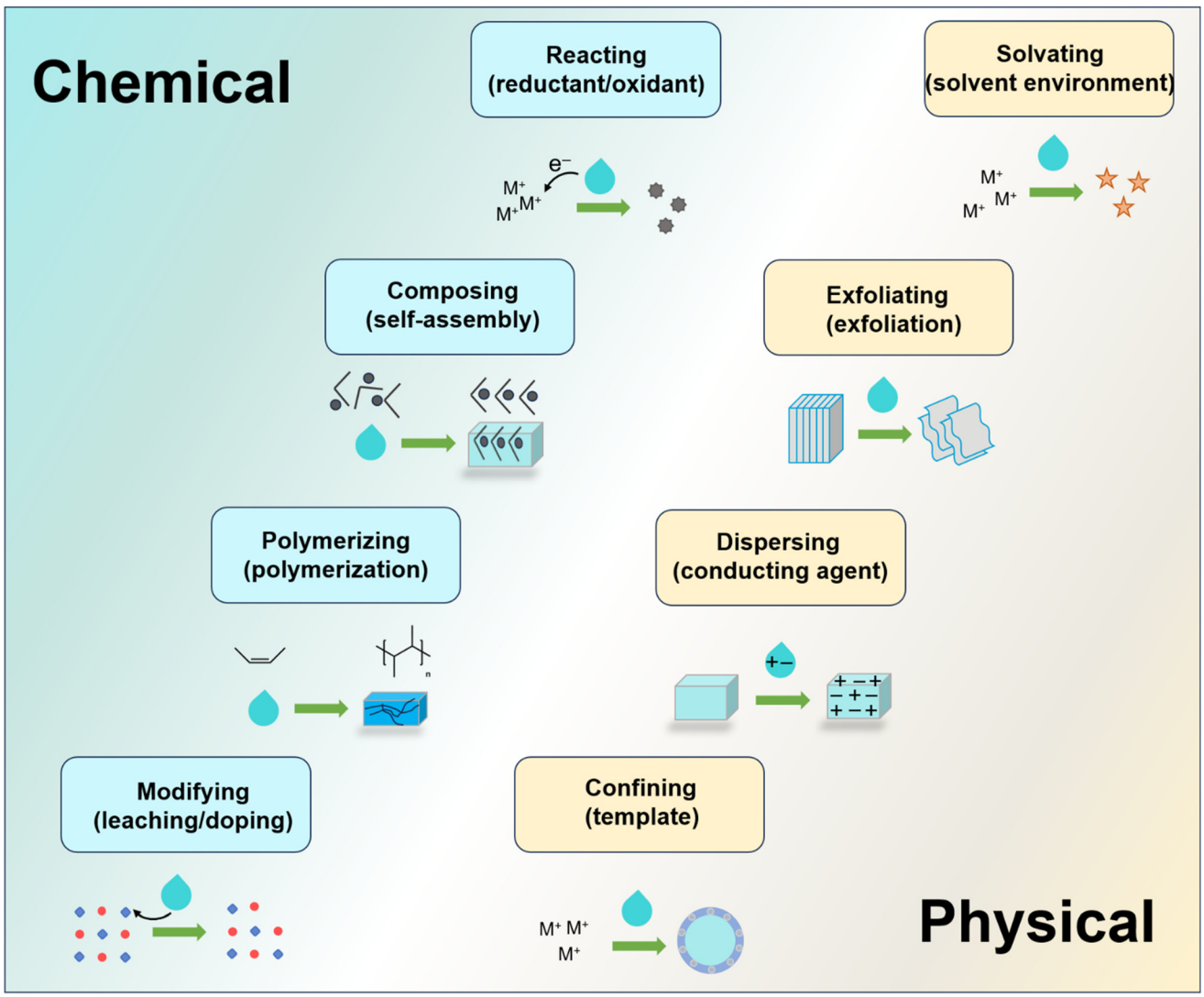

Fig. 13 The role of DESs engaged in material preparation.

the eutectogel give the wood excellent mechanical properties. The prepared material has high transparency (90% light transmittance), good stretchability (strain up to 80%) and high conductivity (0.16 S m^{-1}).

Additionally, this proved that the existence of a solid-like nanofiber network does not significantly inhibit ion transport in DES. The high room temperature ionic conductivity of ChCl/MPG eutectogel places it in the top echelon of gel electrolyte materials and is high enough for possible applications. The hybrid ChCl/MPG eutectogel film exhibits excellent electrochromic activity, making it a good material for fabricating electrochromic devices (ECDs). When the potential increased from 0 to −0.7 V, it changed from light yellow to uniform blue (Fig. 11b). The *in situ* UV-vis transmission spectra of ChCl/MPG ECD at different potentials showed its transmittance decreases with the increase of potential and reaches saturation at −0.7 V when the maximum optical contrast (ΔT_{max}) is 59% (Fig. 11c). The lowest working voltage for ChCl/MPG ECD colouring is −0.4 V, which is much lower than the other semi-solid ECD devices. As is shown in Fig. 11d, the colouring time of ChCl/MPG ECD is about 15 seconds, and the bleaching time is about 30 seconds (time to reach 90% ΔT_{max}). Moreover, ChCl/MPG ECD showed strong cycling performance, maintaining 94.2% of the initial ΔT_{max} after 100 cycles (Fig. 11e). The low working voltage, fast response time and good cycling stability of the prepared ECD prove the possibility of supramolecular eutectogels as next-generation electrolytes for flexible electronic devices.

The above showcased that DES was used to synthesize gel for solid electrolytes, whereas the synthesis method of eutectogel may be different. For example, Smith *et al.* prepared a series of supramolecular eutectogels with ultra-high ionic conductivity by self-assembly.[200] In other cases, the monomers polymerized in DES have changed, leading to the synthesis of diverse eutectogels.[201,202] And there are other methods of forming a framework network, such as the condensation of silica precursors.[8]

Since 2020, the concept of supramolecular DES (SUPRADES) has attracted attention from researchers, while host–guest DES originated earlier.[7,203] This new system retained its inclusion capacity in the resulting solvent, raising a new family of solvent systems. In the case of cyclodextrins (CDs), mixtures of functionalized CDs with hydrogen bond donor species enable an extended liquid-state window. These solvents maintain CD's inclusion capability while also enhancing solvation effectiveness through a prolonged hydrogen bonding network.

Early work focused on the dissolution of CDs in DES, along with their potential applications.[204] For example, Xu *et al.* demonstrated for the first time that hydrophobic DES (methyltrioctylammonium chloride : octanoic acid) can be used for chiral separations in capillary electrophoresis.[205] Optimal conditions were explored: pH 2.5, phosphate buffer containing 1% carboxymethyl-β-CD and 0.15% DES, applied voltage 20 kV. Through this approach, separations of drugs that cannot be accomplished solely within the CD system are successfully attained.

After 2020, CDs have transitioned from their role as solutes to that of solvents.[7,206,207] Guan *et al.* designed CD-based DES (methyl-β-cyclodextrin: formic acid) for catalytic desulfurization of fuel oil.[208] Theoretical calculations and experimental findings have indicated that peroxygen compounds serve as the primary active species, and the remarkable catalytic efficacy of CD-based DESs can reduce the reaction barrier by 81% in the EODS process, achieving an impressive sulfur-removal rate of 99.6%.

7. Outlooks and conclusions

The wide range of materials synthesized using DESs also poses a challenging issue when it comes to scaling up production. In this regard, there have also been some explorations. Cheng *et al.* provided a fast heat exchange and uniform mass transfer process, in which Pd nanocrystals with mainly exposed Pd (100) faces can be synthesized efficiently (Fig. 12a).[209] The expanded hydrogen network and abundant ion species in DES were believed to stabilize the Pd crystal plane and limit the nanocrystal size, which is consistent with reports on the properties of the solvent system.[210] Pd NCs supported on porous carbon exhibited a size distribution of ~13 ± 3.5 nm and a high electrochemical active surface area (46.0 m^2 g^{-1}). Further characterization showed these composite materials have high catalytic performance and excellent stability for the oxidation of formic acid.

The above works demonstrate the extraordinary future of DES as a scalable, sustainable, and high-performance fluid in the flow process to enhance nanomanufacturing efforts. Kim *et al.* synthesized an amorphous $RuCo_2O_4$ nanofiber in a reline–water system.[211] It is worth mentioning that the entire reaction was carried out at 40 °C. Urea underwent a decomposition reaction, and the purported ammonia acted as a reducing agent to react with two salts, which is shown in the following equations:

$$CO(NH_3)_2 \rightarrow NH_3 + HCNO \quad (7)$$

$$RuCl_3 + NH_3 \rightarrow Ru(NH_3)Cl_3 \quad (8)$$

$$Co(NO_3)_2 + NH_3 \rightarrow Co(NH_3)(NO_3)_2 \quad (9)$$

$$Ru(NH_3)Cl_3 + Co(NH_3)(NO_3)_2 + H_2O \rightarrow RuCo_2O_4 + NH_4Cl + NH_4NO_3 \quad (10)$$

Reline and water can lower the total surface energy of the particles produced. The synthesized bimetallic oxide possesses an effective surface area of 245 m^2 g^{-1}, and they were expected to have potential in high-efficiency materials, such as supercapacitors. With the reduction of operating temperature, the cost of the microfluidic method has also been reduced, and shows great application potential in the future.

Another work showed the possibility of low-cost, scalable, controlled size-consistent preparation of nano-catalysts. Li *et al.* used a continuous flow reactor and ethaline to synthesize intermetallic PtPd nanoparticles with controlled shape in

6 minutes.[25] The synthesized PtPd nanocrystals exhibited octahedral shape with mainly exposed (111) facets and an average diameter of 12.8 nm (Fig. 12b). Furthermore, PtPd nanoparticles synthesized by this method are more uniform than particles produced using conventional flask reactors using similar synthesis conditions.

Although DES preparation materials have exhibited some advancements, there are also some problems that need to be solved in this field. First, the kinetic study of the solvothermal growth of materials, including the effects of different temperatures, synthesis time, and monomer composition on the product has been neglected. Second, insight into the transformation process from liquid phase to solid phase during calcination is missing. Third, solvent recycling when preparing materials by electrodeposition is a problem. In addition, AI-assisted research on the properties of DES is considered to have a guiding role in their application.[212]

In 1998, 12 principles of green chemistry were proposed. The description of atom economy is "Synthetic methods should be designed to maximize incorporation of all materials used in the process into the final product".[213] Environmental factor (*E*-factor), which was defined as the following, is believed to be a more accurate measurement of the environmental acceptability of a chemical manufacturing process:[214]

$$E\,\text{factor} = \frac{\text{mass of total waste}}{\text{mass of product}}$$

Despite this, there are relatively few reports on the *E* factor regarding DESs. Researchers have generally discussed the atom economy of reactions involved in DES, which may be because these reactions are mainly at the laboratory scale and in the early stage of industrialization. We believe that as this field develops, atom economics and *E*-factor will become increasingly significant when evaluating cases in DES-chemical manufacturing.

To summarize, DESs participate in the preparation of materials physically or/and chemically. The physical aspect includes solvating, exfoliating, dispersing and confining, while the chemical part includes reacting, composing, polymerizing and modifying (Fig. 13). This review first highlights the heterogeneity of the DES, a characteristic property of this solvent, and explains the origin of good solubility and templating effect. In addition, polarity and solvation properties are discussed as they relate to materials prepared by solvothermal methods; studies of thermal decomposition kinetics are a fundamental aspect of materials prepared by calcination methods, and electrochemical stability is a prerequisite for electrodepositing materials such as metals. Some specific processes in the field of materials preparation are compared, such as intercalation and leaching, doping and compositing, etching and coating. The two opposite processes, top-down and bottom-up, can serve as valuable references when synthesizing materials in a nonaqueous system. Finally, the microfluidic method may provide a possible solution to the scaled-up production of nanomaterials in DESs.

Conflicts of interest

The authors declare no competing interests.

Acknowledgements

This work was supported by the National Natural Science Foundation of China (22238011 and 22073112). D. Y. is thankful for the support from the China Scholarship Council (202006360037). D. J. is thankful for the support from the National Natural Science Foundation of China (U1937601).

References

1 A. P. Abbott, G. Capper, D. L. Davies, R. K. Rasheed and V. Tambyrajah, *Chem. Commun.*, 2003, 70–71.
2 E. L. Smith, A. P. Abbott and K. S. Ryder, *Chem. Rev.*, 2014, **114**, 11060–11082.
3 D. Yu, Z. Xue and T. Mu, *Chem. Soc. Rev.*, 2021, **50**, 8596–8638.
4 D. O. Abranches, M. A. R. Martins, L. P. Silva, N. Schaeffer, S. P. Pinho and J. A. P. Coutinho, *Chem. Commun.*, 2019, **55**, 10253–10256.
5 D. Yu and T. Mu, *J. Phys. Chem. B*, 2019, **123**, 4958–4966.
6 R. Shi, D. Yu, F. Zhou, J. Yu and T. Mu, *Chem. Commun.*, 2022, **58**, 4607–4610.
7 T. El Achkar, T. Moufawad, S. Ruellan, D. Landy, H. Greige-Gerges and S. Fourmentin, *Chem. Commun.*, 2020, **56**, 3385–3388.
8 B. Joos, T. Vranken, W. Marchal, M. Safari, M. K. Van Bael and A. T. Hardy, *Chem. Mater.*, 2018, **30**, 655–662.
9 A. P. Abbott, D. Boothby, G. Capper, D. L. Davies and R. K. Rasheed, *J. Am. Chem. Soc.*, 2004, **126**, 9142–9147.
10 B. B. Hansen, S. Spittle, B. Chen, D. Poe, Y. Zhang, J. M. Klein, A. Horton, L. Adhikari, T. Zelovich, B. W. Doherty, B. Gurkan, E. J. Maginn, A. Ragauskas, M. Dadmun, T. A. Zawodzinski, G. A. Baker, M. E. Tuckerman, R. F. Savinell and J. R. Sangoro, *Chem. Rev.*, 2021, **121**, 1232–1285.
11 P. Y. Chew and A. Reinhardt, *J. Chem. Phys.*, 2023, **158**, 030902.
12 Q. Liu, T. Yuan, Q.-J. Fu, Y.-Y. Bai, F. Peng and C.-L. Yao, *Cellulose*, 2019, **26**, 9447–9462.
13 T. Zhang, T. Doert, H. Wang, S. Zhang and M. Ruck, *Angew. Chem., Int. Ed.*, 2021, **60**, 22148–22165.
14 C. Vidal, J. Garcia-Alvarez, A. Hernan-Gomez, A. R. Kennedy and E. Hevia, *Angew. Chem., Int. Ed.*, 2016, **55**, 16145–16148.
15 H. Vanda, Y. Dai, E. G. Wilson, R. Verpoorte and Y. H. Choi, *C. R. Chim.*, 2018, **21**, 628–638.
16 I. Mamajanov, A. E. Engelhart, H. D. Bean and N. V. Hud, *Angew. Chem., Int. Ed.*, 2010, **49**, 6310–6314.
17 D. Yu, Z. Xue and T. Mu, *Cell Rep. Phys. Sci.*, 2022, **3**, 100809.

18 D. Nakamura, I. Gunjishima, S. Yamaguchi, T. Ito, A. Okamoto, H. Kondo, S. Onda and K. Takatori, *Nature*, 2004, **430**, 1009–1012.
19 E. R. Parnham, E. A. Drylie, P. S. Wheatley, A. M. Z. Slawin and R. E. Morris, *Angew. Chem.*, 2006, **118**, 5084–5088.
20 J. Zhang, T. Wu, S. Chen, P. Feng and X. Bu, *Angew. Chem., Int. Ed.*, 2009, **48**, 3486–3490.
21 H. G. Liao, Y. X. Jiang, Z. Y. Zhou, S. P. Chen and S. G. Sun, *Angew. Chem., Int. Ed.*, 2008, **47**, 9100–9103.
22 O. S. Hammond, K. J. Edler, D. T. Bowron and L. Torrente-Murciano, *Nat. Commun.*, 2017, **8**, 14150.
23 O. S. Hammond, D. T. Bowron and K. J. Edler, *Green Chem.*, 2016, **18**, 2736–2744.
24 M. Zhang, Y.-H. Liu, Z.-R. Shang, H.-C. Hu and Z.-H. Zhang, *Catal. Commun.*, 2017, **88**, 39–44.
25 B. Li, H. Zhang, J. Kaelin, S. Gao, F. Xia, B. An, K. Lu and Y. Cheng, *ACS Appl. Nano Mater.*, 2023, **6**, 3184–3190.
26 S. Datta, J. Mahin, E. Liberti, I. Manasi, K. J. Edler and L. Torrente-Murciano, *ACS Sustainable Chem. Eng.*, 2023, **11**, 10242–10251.
27 O. S. Hammond, R. S. Atri, D. T. Bowron, L. de Campo, S. Diaz-Moreno, L. L. Keenan, J. Doutch, S. Eslava and K. J. Edler, *Nanoscale*, 2021, **13**, 1723–1737.
28 P. C. Jhang, N. T. Chuang and S. L. Wang, *Angew. Chem., Int. Ed.*, 2010, **49**, 4200–4204.
29 B. T. Yonemoto, Z. Lin and F. Jiao, *Chem. Commun.*, 2012, **48**, 9132–9134.
30 K. Y. Wang, D. Ding, S. Zhang, Y. Wang, W. Liu, S. Wang, S. H. Wang, D. Liu and C. Wang, *Chem. Commun.*, 2018, **54**, 4806–4809.
31 Y. Lu, Y. Yang, X. Fan, Y. Li, D. Zhou, B. Cai, L. Wang, K. Fan and K. Zhang, *Adv. Mater.*, 2022, **34**, e2108178.
32 O. S. Hammond, D. T. Bowron and K. J. Edler, *ACS Sustainable Chem. Eng.*, 2019, **7**, 4932–4940.
33 C. D'Agostino, R. C. Harris, A. P. Abbott, L. F. Gladden and M. D. Mantle, *Phys. Chem. Chem. Phys.*, 2011, **13**, 21383–21391.
34 M. E. Di Pietro, O. Hammond, A. van den Bruinhorst, A. Mannu, A. Padua, A. Mele and M. Costa Gomes, *Phys. Chem. Chem. Phys.*, 2021, **23**, 107–111.
35 D. V. Wagle, G. A. Baker and E. Mamontov, *J. Phys. Chem. Lett.*, 2015, **6**, 2924–2928.
36 M. Gilmore, L. M. Moura, A. H. Turner, M. Swadzba-Kwasny, S. K. Callear, J. A. McCune, O. A. Scherman and J. D. Holbrey, *J. Chem. Phys.*, 2018, **148**, 193823.
37 K. Biernacki, H. K. S. Souza, C. M. R. Almeida, A. L. Magalhães and M. P. Gonçalves, *ACS Sustainable Chem. Eng.*, 2020, **8**, 18712–18728.
38 P. Kalhor, K. Ghandi, H. Ashraf and Z. Yu, *Phys. Chem. Chem. Phys.*, 2021, **23**, 13136–13147.
39 A. Faraone, D. V. Wagle, G. A. Baker, E. C. Novak, M. Ohl, D. Reuter, P. Lunkenheimer, A. Loidl and E. Mamontov, *J. Phys. Chem. B*, 2018, **122**, 1261–1267.
40 Y. Zhang, D. Poe, L. Heroux, H. Squire, B. W. Doherty, Z. Long, M. Dadmun, B. Gurkan, M. E. Tuckerman and E. J. Maginn, *J. Phys. Chem. B*, 2020, **124**, 5251–5264.
41 Z. Naseem, R. A. Shehzad, A. Ihsan, J. Iqbal, M. Zahid, A. Pervaiz and G. Sarwari, *Chem. Phys. Lett.*, 2021, **769**, 138427.
42 O. S. Hammond, D. T. Bowron, A. J. Jackson, T. Arnold, A. Sanchez-Fernandez, N. Tsapatsaris, V. Garcia Sakai and K. J. Edler, *J. Phys. Chem. B*, 2017, **121**, 7473–7483.
43 M. Atilhan and S. Aparicio, *J. Phys. Chem. C*, 2018, **122**, 18029–18039.
44 A. Triolo, F. Lo Celso and O. Russina, *J. Phys. Chem. B*, 2020, **124**, 2652–2660.
45 H. Yu, Z. Xue, X. Lan, Q. Liu, R. Shi and T. Mu, *Cellulose*, 2020, **27**, 6175–6188.
46 Q. Liu, X. Zhao, D. Yu, H. Yu, Y. Zhang, Z. Xue and T. Mu, *Green Chem.*, 2019, **21**, 5291–5297.
47 W. Chen, J. Jiang, X. Lan, X. Zhao, H. Mou and T. Mu, *Green Chem.*, 2019, **21**, 4748–4756.
48 A. Pandey, R. Rai, M. Pal and S. Pandey, *Phys. Chem. Chem. Phys.*, 2014, **16**, 1559–1568.
49 M. B. Taysun, E. Sert and F. S. Atalay, *J. Chem. Eng. Data*, 2017, **62**, 1173–1181.
50 M. Q. Farooq, G. A. Odugbesi, N. M. Abbasi and J. L. Anderson, *ACS Sustainable Chem. Eng.*, 2020, **8**, 18286–18296.
51 C. Florindo, A. J. S. McIntosh, T. Welton, L. C. Branco and I. M. Marrucho, *Phys. Chem. Chem. Phys.*, 2017, **20**, 206–213.
52 J. L. Anderson, J. Ding, T. Welton and D. W. Armstrong, *J. Am. Chem. Soc.*, 2002, **124**, 14247–14254.
53 M. H. Abraham, *Chem. Soc. Rev.*, 1993, **22**, 73–83.
54 A. Valvi, J. Dutta and S. Tiwari, *J. Phys. Chem. B*, 2017, **121**, 11356–11366.
55 A. R. R. Teles, E. V. Capela, R. S. Carmo, J. A. P. Coutinho, A. J. D. Silvestre and M. G. Freire, *Fluid Phase Equilib.*, 2017, **448**, 15–21.
56 A. Sanchez-Fernandez, K. J. Edler, T. Arnold, D. Alba Venero and A. J. Jackson, *Phys. Chem. Chem. Phys.*, 2017, **19**, 8667–8670.
57 L. Das and S. Adhikari, *J. Phys. Chem. B*, 2018, **122**, 8900–8907.
58 F. Milano, L. Giotta, M. R. Guascito, A. Agostiano, S. Sblendorio, L. Valli, F. M. Perna, L. Cicco, M. Trotta and V. Capriati, *ACS Sustainable Chem. Eng.*, 2017, **5**, 7768–7776.
59 F. Zhen, L. Percevault, L. Paquin, E. Limanton, C. Lagrost and P. Hapiot, *J. Phys. Chem. B*, 2020, **124**, 1025–1032.
60 J. A. McCune, M. F. Kuehnel, E. Reisner and O. A. Scherman, *Chem*, 2020, **6**, 1819–1830.
61 S. Kaur, A. Gupta and H. K. Kashyap, *J. Phys. Chem. B*, 2016, **120**, 6712–6720.
62 V. Alizadeh, D. Geller, F. Malberg, P. B. Sanchez, A. Padua and B. Kirchner, *ChemPhysChem*, 2019, **20**, 1786–1792.
63 A. Felipe, C. A. Lovenduski, J. L. Baker and G. E. Lindberg, *Phys. Chem. Chem. Phys.*, 2022, **24**, 13720–13729.
64 S. Spittle, D. Poe, B. Doherty, C. Kolodziej, L. Heroux, M. A. Haque, H. Squire, T. Cosby, Y. Zhang, C. Fraenza, S. Bhattacharyya, M. Tyagi, J. Peng, R. A. Elgammal,

T. Zawodzinski, M. Tuckerman, S. Greenbaum, B. Gurkan, C. Burda, M. Dadmun, E. J. Maginn and J. Sangoro, *Nat. Commun.*, 2022, **13**, 219.
65 R. Maglia de Souza, M. Karttunen and M. C. C. Ribeiro, *J. Chem. Inf. Model.*, 2021, **61**, 5938–5947.
66 Y. Cui and D. G. Kuroda, *J. Phys. Chem. A*, 2018, **122**, 1185–1193.
67 S. McDonald, T. Murphy, S. Imberti, G. G. Warr and R. Atkin, *J. Phys. Chem. Lett.*, 2018, **9**, 3922–3927.
68 S. Zhang, R. Shi, X. Ma, L. Lu, Y. He, X. Zhang, Y. Wang and Y. Deng, *Chem. – Eur. J.*, 2012, **18**, 11904–11908.
69 S. Chatterjee, T. Haldar, D. Ghosh and S. Bagchi, *J. Phys. Chem. B*, 2020, **124**, 3709–3715.
70 A. Malik and H. K. Kashyap, *Phys. Chem. Chem. Phys.*, 2021, **23**, 3915–3924.
71 L. Percevault, A. Jani, T. Sohier, L. Noirez, L. Paquin, F. Gauffre and D. Morineau, *J. Phys. Chem. B*, 2020, **124**, 9126–9135.
72 N. Subba, E. Tarif, P. Sen and R. Biswas, *J. Phys. Chem. B*, 2020, **124**, 1995–2005.
73 S. Banerjee, P. K. Ghorai, S. Das, J. Rajbangshi and R. Biswas, *J. Chem. Phys.*, 2020, **153**, 234502.
74 S. Kaur, S. Sharma and H. K. Kashyap, *J. Chem. Phys.*, 2017, **147**, 194507.
75 M. H. Mamme, S. L. C. Moors, H. Terryn, J. Deconinck, J. Ustarroz and F. De Proft, *J. Phys. Chem. Lett.*, 2018, **9**, 6296–6304.
76 J. J. Buzolic, H. Li, Z. M. Aman, G. G. Warr and R. Atkin, *J. Colloid Interface Sci.*, 2022, **616**, 121–128.
77 S. Panda, K. Kundu, J. Kiefer, S. Umapathy and R. L. Gardas, *J. Phys. Chem. B*, 2019, **123**, 3359–3371.
78 X. Lan, X. Wang, W. Du, T. Mu and X. Z. Lan, *Phys. Chem. Chem. Phys.*, 2021, **23**, 13785–13788.
79 S. S. Hossain, S. Paul and A. Samanta, *J. Phys. Chem. B*, 2019, **123**, 6842–6850.
80 S. S. Hossain and A. Samanta, *Phys. Chem. Chem. Phys.*, 2018, **20**, 24613–24622.
81 S. Chatterjee, D. Ghosh, T. Haldar, P. Deb, S. S. Sakpal, S. H. Deshmukh, S. M. Kashid and S. Bagchi, *J. Phys. Chem. B*, 2019, **123**, 9355–9363.
82 L. Kollau, R. Tuinier, J. Verhaak, J. den Doelder, I. A. W. Filot and M. Vis, *J. Phys. Chem. B*, 2020, **124**, 5209–5219.
83 Y. Hou, B. Zhang, M. Gao, S. Ren and W. Wu, *J. Chem. Thermodyn.*, 2023, **179**, 106999.
84 C. Vidal, J. Garcia-Alvarez, A. Hernan-Gomez, A. R. Kennedy and E. Hevia, *Angew. Chem., Int. Ed.*, 2014, **53**, 5969–5973.
85 W. Chen, Z. Xue, J. Wang, J. Jiang, X. Zhao and T. Mu, *Acta Phys.-Chim. Sin.*, 2018, **34**, 904–911.
86 B. Janković, N. Manić, I. Perović, M. Vujković and N. Zdolšek, *J. Mol. Liq.*, 2023, **374**, 121274.
87 C. Florindo, F. S. Oliveira, L. P. N. Rebelo, A. M. Fernandes and I. M. Marrucho, *ACS Sustainable Chem. Eng.*, 2014, **2**, 2416–2425.
88 S. Liu, D. Yu, Y. Chen, R. Shi, F. Zhou and T. Mu, *Ind. Eng. Chem. Res.*, 2022, **61**, 14347–14354.
89 Y. Chen, D. Yu, L. Fu, M. Wang, D. Feng, Y. Yang, X. Xue, J. Wang and T. Mu, *Phys. Chem. Chem. Phys.*, 2019, **21**, 11810–11821.
90 S. Kaur and H. K. Kashyap, *J. Phys. Chem. B*, 2018, **122**, 5242–5250.
91 Q. Li, J. Jiang, G. Li, W. Zhao, X. Zhao and T. Mu, *Sci. China: Chem.*, 2016, **59**, 571–577.
92 L. Das, S. Mukherjee, D. Kumar Maity and S. Adhikari, *J. Mol. Liq.*, 2022, **360**, 119377.
93 Z. Xue, L. Qin, J. Jiang, T. Mu and G. Gao, *Phys. Chem. Chem. Phys.*, 2018, **20**, 8382–8402.
94 A. Kityk, P. Švec, J. Šoltys, V. Pavlik and M. Hnatko, *J. Mol. Liq.*, 2023, **375**, 121316.
95 A. Pandey and S. Pandey, *J. Phys. Chem. B*, 2014, **118**, 14652–14661.
96 O. Longeras, A. Gautier, K. Ballerat-Busserolles and J.-M. Andanson, *ACS Sustainable Chem. Eng.*, 2020, **8**, 12516–12520.
97 S. Chen, J. Zhang, T. Wu, P. Feng and X. Bu, *Dalton Trans.*, 2010, **39**, 697–699.
98 J. Qiu, P. Guan, Y. Zhao, Z. Li, H. Wang and J. Wang, *Green Chem.*, 2020, **22**, 7537–7542.
99 S. D. Çalhan, M. Ö. Alaş, M. Aşık, F. N. D. Kaya and R. Genç, *J. Mater. Sci.*, 2018, **53**, 15362–15375.
100 X. Zhao, X. Lan, D. Yu, H. Fu, Z. Liu and T. Mu, *Chem. Commun.*, 2018, **54**, 13010–13013.
101 J. Jiang, C. Yan, X. Zhao, H. Luo, Z. Xue and T. Mu, *Green Chem.*, 2017, **19**, 3023–3031.
102 S. Datta, C. Jo, M. De Volder and L. Torrente-Murciano, *ACS Appl. Mater. Interfaces*, 2020, **12**, 18803–18812.
103 S. Kumar-Krishnan, R. Esparza and U. Pal, *ACS Omega*, 2020, **5**, 3699–3708.
104 H. Lei, S. Singh Siwal, X. Zhang and Q. Zhang, *J. Colloid Interface Sci.*, 2020, **571**, 1–12.
105 O. Oderinde, M. Kang, M. Kalulu, F. Yao and G. Fu, *Superlattices Microstruct.*, 2019, **125**, 103–112.
106 P. Jittiarporn, L. Sikong, K. Kooptarnond, W. Taweepreda, S. Stoenescu, S. Badilescu and V.-V. Truong, *Surf. Coat. Technol.*, 2017, **327**, 66–74.
107 D. P. Jaihindh, A. Manikandan, Y. L. Chueh and Y. P. Fu, *ChemSusChem*, 2020, **13**, 2726–2738.
108 B. Sriram, J. N. Baby, S.-F. Wang, M. R. Ranjitha, M. Govindasamy and M. George, *ACS Sustainable Chem. Eng.*, 2020, **8**, 17772–17782.
109 L. Ding, Z. Li, L. Chen and Z. Qi, *Electrochim. Acta*, 2023, **455**, 142424.
110 D. Xue, D. Zhu, H. Duan, Z. Wang, Y. Lv, W. Xiong, L. Li, M. Liu and L. Gan, *Chem. Commun.*, 2019, **55**, 11219–11222.
111 M. T. Vallejo-Macías, C. L. Recio-Colmenares, J. B. Pelayo-Vázquez, S. Gómez-Salazar, F. Carvajal-Ramos, J. F. Soltero-Martínez, M. Vázquez-Lepe, J. D. Mota-Morales and M. G. Pérez-García, *ACS Appl. Nano Mater.*, 2020, **3**, 5794–5806.
112 O. S. Hammond, D. T. Bowron and K. J. Edler, *Angew. Chem., Int. Ed.*, 2017, **56**, 9782–9785.

113 W. Liu, Y. Yu, L. Cao, G. Su, X. Liu, L. Zhang and Y. Wang, *J. Hazard. Mater.*, 2010, **181**, 1102–1108.
114 Q. Wang, B. Dong, Y. Zhao, F. Huang, J. Xie, G. Cui and B. Tang, *Chem. Eng. J.*, 2018, **348**, 811–819.
115 M. Karimi and M. J. Eshraghi, *J. Alloys Compd.*, 2017, **696**, 171–176.
116 K. Aruchamy, R. N. Maalige, M. M. Halanur, A. Mahto, R. Nagaraj, D. Kalpana, D. Ghosh, D. Mondal and S. K. Nataraj, *Chem. Eng. J.*, 2020, **379**, 112327.
117 M. Starykevich, A. N. Salak, D. K. Ivanou, K. A. Yasakau, P. S. André, R. A. S. Ferreira, M. L. Zheludkevich and M. G. S. Ferreira, *J. Electrochem. Soc.*, 2017, **164**, D88–D94.
118 V. S. Cvetković, N. M. Vukićević, N. Jovićević, J. S. Stevanović and J. N. Jovićević, *Trans. Nonferrous Met. Soc. China*, 2020, **30**, 823–834.
119 J. Wang, P. Wang, Q. Wang, H. Mou, B. Cao, D. Yu, D. Wang, S. Zhang and T. Mu, *ACS Sustainable Chem. Eng.*, 2018, **6**, 15480–15486.
120 E. Gunnell, A. Avery, L. Gunnell, M. Spotts, M. Stoddard and J. N. Harb, *J. Electrochem. Soc.*, 2021, **168**, 046501.
121 L. Wei, C.-D. Xu, L. Huang, Z.-Y. Zhou, S.-P. Chen and S.-G. Sun, *J. Phys. Chem. C*, 2015, **120**, 15569–15577.
122 A. Bordet, S. El Sayed, M. Sanger, K. J. Boniface, D. Kalsi, K. L. Luska, P. G. Jessop and W. Leitner, *Nat. Chem.*, 2021, **13**, 916.
123 R. Bernasconi, A. Lucotti, L. Nobili and L. Magagnin, *J. Electrochem. Soc.*, 2018, **165**, D620–D627.
124 Z. Su, C. Xu, Y. Hua, J. Li, J. Ru, M. Wang, L. Xiong and Y. Zhang, *Int. J. Electrochem. Sci.*, 2016, **11**, 3311.
125 G.-F. Cai, J.-P. Tu, C.-D. Gu, J.-H. Zhang, J. Chen, D. Zhou, S.-J. Shi and X.-L. Wang, *J. Mater. Chem. A*, 2013, **1.**, 4286–4292.
126 L. Chen, J. Zeng, M. Guo, R. Xue, R. Deng and Q. Zhang, *J. Colloid Interface Sci.*, 2021, **583**, 594–604.
127 C. Yang, T. He, W. Zhou, R. Deng and Q. Zhang, *ACS Sustainable Chem. Eng.*, 2020, **8**, 13793–13804.
128 K. Li, T.-Z. Ren, Z.-Y. Yuan and T. J. Bandosz, *Int. J. Hydrogen Energy*, 2018, **43**, 10448–10457.
129 A. P. Abbott, M. Azam, K. S. Ryder and S. Saleem, *Trans. IMF*, 2018, **96**, 297–303.
130 A. D. Ballantyne, G. C. Forrest, G. Frisch, J. M. Hartley and K. S. Ryder, *Phys. Chem. Chem. Phys.*, 2015, **17**, 30540–30550.
131 S.-P. Wang, Y.-Y. Hsieh, P.-Y. Chen and I. W. Sun, *J. Electrochem. Soc.*, 2019, **166**, D768–D775.
132 E. Gutierrez, J. A. Rodriguez, J. Cruz-Borbolla, Y. Castrillejo and E. Barrado, *Int. J. Electrochem. Sci.*, 2018, **13**, 11016–11023.
133 L. Anicai, S. Costovici, A. Cojocaru, A. Manea and T. Visan, *Trans. IMF*, 2016, **93**, 302–312.
134 V. S. Protsenko, L. S. Bobrova, S. A. Korniy, A. A. Kityk and F. I. Danilov, *Funct. Mater.*, 2018, **25**, 539–545.
135 P. Sebastián, E. Gómez, V. Climent and J. M. Feliu, *Electrochem. Commun.*, 2017, **78**, 51–55.
136 M. A. Miller, J. S. Wainright and R. F. Savinell, *J. Electrochem. Soc.*, 2017, **164**, A796–A803.
137 M. Steichen, M. Thomassey, S. Siebentritt and P. J. Dale, *Phys. Chem. Chem. Phys.*, 2011, **13**, 4292–4302.
138 R. Bernasconi and L. Magagnin, *J. Optoelectron. Adv. Mater.*, 2015, **17**, 122–126.
139 M. W. Guo, C. B. Sun, W. Q. Yang, L. Chen, H. Lei and Q. B. Zhang, *Electrochim. Acta*, 2020, **341**, 136017.
140 R. Kang, M. An, F. Cui, J. Wang and J. Liang, *Mater. Res. Express*, 2019, **6**, 1165a6.
141 Y.-S. Liao, P.-Y. Chen and I. W. Sun, *Electrochim. Acta*, 2016, **214**, 265–275.
142 F. Soma, Q. Rayée, M. Bougouma, C. Baustert, C. Buess-Herman and T. Doneux, *Electrochim. Acta*, 2020, **345**, 136165.
143 L. Wei, Y.-J. Fan, H.-H. Wang, N. Tian, Z.-Y. Zhou and S.-G. Sun, *Electrochim. Acta*, 2012, **76**, 468–474.
144 M. Jayakumar, C. Murugesan, C. Andrew, K. Natarajan and R. Sekar, *J. Electrochem. Soc.*, 2022, **169**, 032510.
145 J. Bu, J. Ru, Z. Wang, Y. Hua, C. Xu, Y. Zhang and Y. Wang, *Adv. Powder Technol.*, 2019, **30**, 2859–2867.
146 E. Gómez, P. Cojocaru, L. Magagnin and E. Valles, *J. Electroanal. Chem.*, 2011, **658**, 18–24.
147 Z. Wang, J. Ru, Y. Hua, D. Wang and J. Bu, *J. Electrochem. Soc.*, 2020, **167**, 082504.
148 A. P. Abbott, J. C. Barron, G. Frisch, S. Gurman, K. S. Ryder and A. Fernando Silva, *Phys. Chem. Chem. Phys.*, 2011, **13**, 10224–10231.
149 P.-K. Wang, W.-J. Lin and I. W. Sun, *J. Electrochem. Soc.*, 2019, **166**, D374–D380.
150 B. Bozzini, B. Busson, C. Humbert, C. Mele and A. Tadjeddine, *Electrochim. Acta*, 2016, **218**, 208–215.
151 Y. S. Gao, W. C. Hu, X. Q. Gao and B. X. Duan, *Surf. Eng.*, 2013, **28**, 590–593.
152 K. Kopczyński and G. Lota, *Electrochem. Commun.*, 2019, **107**, 106538.
153 G. Saravanan and S. Mohan, *J. Alloys Compd.*, 2012, **522**, 162–166.
154 S.-L. Wang, J.-B. Lin, Q.-Y. Cai and Y. Zhang, *J. Alloys Compd.*, 2008, **450**, 142–147.
155 A. Liu, Z. Shi and R. G. Reddy, *Metall. Mater. Trans. B*, 2020, **51**, 1162–1168.
156 W.-S. Chiang, J.-Q. Huang, P.-C. Chen, P.-W. Wu, A. Joi and Y. Dordi, *J. Alloys Compd.*, 2018, **742**, 38–44.
157 S. Geng, H. Dong, Y. Lu, S. Wang, Y. Huang, X. Zou, Y. Zhang, Q. Xu and X. Lu, *Sep. Purif. Technol.*, 2020, **242**, 116779.
158 X. Xie, X. Zou, X. Lu, Q. Xu, C. Lu, C. Chen and Z. Zhou, *J. Appl. Electrochem.*, 2017, **47**, 679–689.
159 T. Yanai, K. Shiraishi, Y. Watanabe, T. Ohgai, M. Nakano, K. Suzuki and H. Fukunaga, *J. Appl. Phys.*, 2015, **117**, 17A925.
160 Z. Wang, T. Wu, J. Ru, Y. Hua, J. Bu and D. Wang, *Surf. Coat. Technol.*, 2021, **406**, 126636.
161 J. Li, H. Lai, B. Fan, B. Zhuang, L. Guan and Z. Huang, *J. Alloys Compd.*, 2009, **477**, 547–551.
162 Y. You, C. Gu, X. Wang and J. Tu, *J. Electrochem. Soc.*, 2012, **159**, D642–D648.

163 V. R. C. Thanu, C. Andrew and M. Jayakumar, *Surf. Interfaces*, 2020, **19**, 100539.
164 M. Manolova, R. Böck, I. Scharf, T. Mehner and T. Lampke, *J. Alloys Compd.*, 2021, **855**, 157462.
165 L. Vieira, J. Burt, P. W. Richardson, D. Schloffer, D. Fuchs, A. Moser, P. N. Bartlett, G. Reid and B. Gollas, *ChemistryOpen*, 2017, **6**, 393–401.
166 L. Anicai, A. Petica, S. Costovici, C. Moise, O. Brincoveanu and T. Visan, *Coatings*, 2019, **9**, 800.
167 M. Bučko, D. Culliton, A. J. Betts and J. B. Bajat, *Trans. IMF*, 2017, **95**, 60–64.
168 C. Xu, Q. Wu, Y. Hua and J. Li, *J. Solid State Electrochem.*, 2014, **18**, 2149–2155.
169 M. Li, B. Q. Chen, T. T. Xiong, L. X. Gao, C. Du, Y. N. Zhu and S. M. Zhang, *J. Dispersion Sci. Technol.*, 2019, **41**, 941–947.
170 S. Fashu, L. Mudzingwa, R. Khan and M. Tozvireva, *Trans. IMF*, 2017, **96**, 20–26.
171 A. Renjith and V. Lakshminarayanan, *ACS Appl. Nano Mater.*, 2020, **3**, 2705–2712.
172 S. Kumaraguru, R. Pavulraj, J. Vijayakumar and S. Mohan, *J. Alloys Compd.*, 2017, **693**, 1143–1149.
173 R. Li, Y. Hou and J. Liang, *Appl. Surf. Sci.*, 2016, **367**, 449–458.
174 W. Q. Yang, Y. X. Hua, Q. B. Zhang, H. Lei and C. Y. Xu, *Electrochim. Acta*, 2018, **273**, 71–79.
175 L. Juárez-Marmolejo, B. Maldonado-Teodocio, M. G. Montes de Oca-Yemha, M. Romero-Romo, M. T. Ramírez-Silva, E. M. Arce-Estrada, P. Morales-Gil, J. Mostany and M. Palomar-Pardavé, *J. Electrochem. Soc.*, 2020, **167**, 112509.
176 A. Renjith and V. Lakshminarayanan, *J. Mater. Chem. A*, 2015, **3**, 3019–3028.
177 D. Xu, Y. Yang, B. Zhang, Z. Yang, S. Liu and T. Mu, *ChemSusChem*, 2022, **15**, e202200822.
178 H. Hu, S. Guo, Y. Wang and K. Shi, *J. Electrochem. Soc.*, 2020, **167**, 166512.
179 O. I. Zaytsev, M. R. Ehrenburg, E. B. Molodkina, P. Broekmann and A. V. Rudnev, *J. Electroanal. Chem.*, 2022, **926**, 116940.
180 S. Wang, X. Xiong, X. Zou, K. Ding, Z. Pang, Q. Xu, Z. Zhou and X. Lu, *J. Mater. Chem. A*, 2020, **8**, 4354–4361.
181 C. Zhang, Y. Jia, Y. Jing, H. Wang and K. Hong, *J. Mol. Model.*, 2014, **20**, 2374.
182 R. Gupta, J. Gamare, M. Sahu, K. Pandey and S. K. Gupta, *J. Mol. Liq.*, 2021, **329**, 115550.
183 R. Zhou, C. Xu, J. Yang, D. Guan and J. Cai, *Chem. Lett.*, 2020, **49**, 585–588.
184 D.-W. Lee, M.-H. Jin, J.-H. Park, Y.-J. Lee, Y.-C. Choi, J. Chan Park and D. H. Chun, *ACS Sustainable Chem. Eng.*, 2018, **6**, 12241–12250.
185 H. Mou, J. Wang, D. Yu, D. Zhang, F. Lu, L. Chen, D. Wang and T. Mu, *J. Mater. Chem. A*, 2019, **7**, 13455–13459.
186 G. M. Thorat, H. S. Jadhav, W.-J. Chung and J. G. Seo, *J. Alloys Compd.*, 2018, **732**, 694–704.
187 F. Jiang, Y. Zhou, J. Su, Y.-F. Long, X.-Y. Lv and Y.-X. Wen, *Ionics*, 2020, **26**, 5553–5563.
188 A. Verma, D. P. Jaihindh and Y. P. Fu, *Dalton Trans.*, 2019, **48**, 8594–8610.
189 H. Mou, J. Wang, D. Yu, D. Zhang, W. Chen, Y. Wang, D. Wang and T. Mu, *ACS Appl. Mater. Interfaces*, 2019, **11**, 44360–44365.
190 J. Wang, H. Mou, R. Li, Y. Li, D. Wang, Z. Xue and T. Mu, *Green Chem.*, 2018, **20**, 5266–5270.
191 R. Boston, P. Y. Foeller, D. C. Sinclair and I. M. Reaney, *Inorg. Chem.*, 2017, **56**, 542–547.
192 J. N. Baby, B. Sriram, S.-F. Wang and M. George, *ACS Sustainable Chem. Eng.*, 2020, **8**, 1479–1486.
193 X. Zhao, Y. Zhou, A.-L. Jin, K. Huang, F. Liu and D.-J. Tao, *New J. Chem.*, 2018, **42**, 15871–15878.
194 H. Ying, J. Bi, H. Xu, G. Wu, X. Wu, J. Hao and Z. Li, *ACS Sustainable Chem. Eng.*, 2022, **10**, 6766–6774.
195 Y. Wei, J. Jiang, J. Dong, Y. Xu, J. Fu and Q. Xu, *Green Chem.*, 2022, **24**, 8014–8020.
196 S. K. Shinde, S. S. Karade, N. C. Maile, H. M. Yadav, A. D. Jagadale, M. B. Jalak and D. Y. Kim, *Int. J. Energy Res.*, 2022, **46**, 16693–16715.
197 Q. Shan, Q. Ding, X. Wang and W. Wu, *Langmuir*, 2022, **38**, 8169–8178.
198 C. Gu, Y. Peng, J. Li, H. Wang, X. Q. Xie, X. Cao and C. S. Liu, *Angew. Chem., Int. Ed.*, 2020, **59**, 18768–18773.
199 M. Wang, R. Li, G. Chen, S. Zhou, X. Feng, Y. Chen, M. He, D. Liu, T. Song and H. Qi, *ACS Appl. Mater. Interfaces*, 2019, **11**, 14313–14321.
200 J. Ruiz-Olles, P. Slavik, N. K. Whitelaw and D. K. Smith, *Angew. Chem., Int. Ed.*, 2019, **58**, 4173–4178.
201 M. W. Logan, S. Langevin, B. Tan, A. W. Freeman, C. Hoffman, D. B. Trigg and K. Gerasopoulos, *J. Mater. Chem. A*, 2020, **8**, 8485–8495.
202 C. Wang, H. Zhang, S. Dong, Z. Hu, R. Hu, Z. Guo, T. Wang, G. Cui and L. Chen, *Chem. Mater.*, 2020, **32**, 9167–9175.
203 D. Yu, H. Mou, H. Fu, X. Lan, Y. Wang and T. Mu, *Chem. – Asian J.*, 2019, **14**, 4183–4188.
204 P. Janicka, M. Kaykhaii, J. Płotka-Wasylka and J. Gębicki, *Green Chem.*, 2022, **24**, 5035–5045.
205 Y. Xu, A. Li, S. Xue, S. Ding and Q. Zhang, *Talanta*, 2023, **260**, 124556.
206 S. Wu, C. Cai, F. Li, Z. Tan and S. Dong, *Angew. Chem., Int. Ed.*, 2020, **59**, 11871–11875.
207 Z.-H. Cai, J.-D. Wang, L. Liu, L.-D. Ruan, Q. Gu, X.-Y. Yan, L.-N. Fu, P.-Q. Zhao, S. Zhang and Y.-J. Fu, *Chem. Eng. J.*, 2023, **457.**, 141333.
208 S. Guan, Z. Li, B. Xu, J. Wu, N. Wang, J. Zhang, J. Han, T. Guan, J. Wang and K. Li, *Chem. Eng. J.*, 2022, **441.**, 136022.
209 H. Zhang, K. Lu, B. Li, Y. Liu, Y. Su, R. Wang and Y. Cheng, *ACS Appl. Mater. Interfaces*, 2020, **12**, 42704–42710.
210 C. R. Ashworth, R. P. Matthews, T. Welton and P. A. Hunt, *Phys. Chem. Chem. Phys.*, 2016, **18**, 18145–18160.

211 S. S. Karade, S. Lalwani, J.-H. Eum and H. Kim, *Sustainable Energy Fuels*, 2020, **4**, 3066–3076.
212 D. Shi, F. Zhou, W. Mu, C. Ling, T. Mu, G. Yu and R. Li, *Phys. Chem. Chem. Phys.*, 2022, **24**, 26029–26036.
213 P. T. Anastas and J. C. Warner, *Green Chemistry: Theory and Practice*, Oxford University Press, New York, 1998.
214 R. A. Sheldon, *Green Chem.*, 2017, **19**, 18–43.